ADVANCING EARTH AND SPACE SCIENCES

JGR Solid Earth

RESEARCH ARTICLE
10.1029/2024JB030688

Key Points:

- Due to the large offset of Romanche transform fault the cold edge effect at the intersection with the Mid-Atlantic Ridge extends for 80 km
- Despite the extreme cooling, volcanic structures are observed along the ridge axis as close as 10 km from the Ridge-Transform Intersection
- The orientation of faults and volcanic structures depends on the: lithosphere thickness, component of shear stress and local magma supply

Supporting Information:

Supporting Information may be found in the online version of this article.

Correspondence to:

L. Grenet,
leagrenet12@gmail.com

Citation:

Grenet, L., Maia, M., Hamelin, C., Briais, A., Guillou, H., Scao, V., & Brunelli, D. (2025). A deep dive into a ridge-transform fault intersection: Volcano-tectonic relationships in an enhanced cold-edge effect at the Romanche fracture zone. *Journal of Geophysical Research: Solid Earth*, *130*, e2024JB030688. https://doi.org/10.1029/2024JB030688

Received 12 NOV 2024
Accepted 4 APR 2025

Author Contributions:

Conceptualization: Marcia Maia, Cédric Hamelin
Formal analysis: Léa Grenet, Hervé Guillou, Vincent Scao
Funding acquisition: Marcia Maia, Daniele Brunelli
Investigation: Léa Grenet
Methodology: Léa Grenet, Marcia Maia, Cédric Hamelin, Anne Briais, Hervé Guillou
Project administration: Marcia Maia
Supervision: Marcia Maia, Cédric Hamelin, Anne Briais
Writing – original draft: Léa Grenet

A Deep Dive Into a Ridge-Transform Fault Intersection: Volcano-Tectonic Relationships in an Enhanced Cold-Edge Effect at the Romanche Fracture Zone

Léa Grenet[1,2], Marcia Maia[1], Cédric Hamelin[3], Anne Briais[1], Hervé Guillou[4], Vincent Scao[4], and Daniele Brunelli[5,6]

[1]Geo-Ocean, UMR6538 CNRS-IFREMER-UBO-UBS Institut, Universitaire Européen de la Mer IUEM, Brest, France, [2]Now at Université de La Réunion, Laboratoire GéoSciences Réunion, Saint Denis, France, [3]Independent scholar, Søndre Skogveien 7, Bergen, Norway, [4]Laboratoire des Sciences du Climat et de l'Environnement, LSCE/IPSL, CEA-CNRS-UVSQ, Université Paris-Saclay, Gif-sur-Yvette, France, [5]Dipartimento di Scienze Chimiche e Geologiche, Università di Modena e Reggio Emilia, Modena, Italy, [6]Woods Hole Oceanographic Institution, Woods Hole, MA, USA

Abstract At mid-ocean ridges, the mantle temperature and composition, and the lithosphere thickness control the melting conditions, which influence the feeding and structure of the neo-volcanic areas. We present a study of the eastern intersection between the Romanche transform fault (TF) and the adjacent southward segments of the Mid-Atlantic Ridge (MAR). A strong thermal gradient is expected along the axis. We focus on the construction of the axial domain and on the spatial and temporal volcano-tectonic interplays. The geological mapping of the intersection shows a progressive variation in the orientation of the normal faults from about 30° to 90° oblique to the spreading direction with increasing distance from the TF. This attests to the decrease of the transform-related shear stress component and the thinning of the axial lithosphere southward. Contextually, the coupled thermal edge effect influences the effusion rate and magma supply which in this area are low compared to other MAR segments. However, recent volcanic activity along the axis starts about 10 km south of the ridge-transform intersection. Rather than a progressive increase of the magma supply with the distance from the TF, the volcanic activity seems to increase abruptly about 30 km south of the intersection. The segment RC2, from ~30 to 55 km from the Romanche TF, displays more numerous and larger seamounts than the segment RC3 located ~80 km from the TF, an observation which we interpret to result from the increased thickness of the lithosphere under RC2, due to its proximity with the ridge-transform intersection.

Plain Language Summary The oceanic crust forms at mid-ocean ridges by partial melting of the Earth's mantle. The morphology of the ridge axis varies with the amount of magma supplied to the ridge which depends mainly on the mantle temperature and lithosphere thickness. To better understand the construction modes of mid-ocean ridges, we studied the eastern intersection between the Romanche transform fault (TF) and the adjacent southward segment of the Mid-Atlantic Ridge. In this area the mantle temperature strongly decreases near the TF, because the hot mantle under the ridge becomes in contact with the cold, old lithosphere. We mapped the seafloor, identified faults, measured the volcano size, estimated the sedimentary cover and dated samples of basalts to define the timing of some volcanic eruptions. Despite the cold mantle, volcanic activity was observed all along the ridge axis, even close to the TF. The volcanic segment closest to the TF appears to have larger and more numerous seamounts than the one located farther away. The direction of faults changes, becoming less oblique to spreading with distance from the TF. We interpret both observations to result from the thinning of the axial lithosphere with increasing distance from the TF.

1. Introduction

At mid-ocean ridges (MOR), the temperature of the mantle controls the lithospheric thickness, the magma supply and the structure of the neo-volcanic zone (NVZ) (Klein & Langmuir, 1987; Langmuir et al., 1992; Phipps Morgan & Chen, 1993). Deepening earthquakes along MORs suggest that the lithosphere thickness increases with decreasing spreading rate (Grevemeyer et al., 2019; Huang & Solomon, 1988). The morphology of slow-spreading mid-ocean ridges is characterized by a wide and deep axial valley including an axial volcanic ridge (AVR) and individual volcanoes (Macdonald & Luyendyk, 1977; Tapponnier & Francheteau, 1978). The accretion at slow-spreading ridges appears to be cyclical, alternating between phases of magmatic construction, characterized by the formation of volcanoes and narrow volcanic ridges, and phases of tectonic destruction, when

Writing – review & editing:
Marcia Maia, Cédric Hamelin,
Anne Briais, Hervé Guillou, Vincent Scao,
Daniele Brunelli

the seafloor is affected by faults and the volcanic constructions are split (Briais et al., 2000; Mendel et al., 2003; Parson et al., 1993; Peirce et al., 2005). The intermittent magmatic supply and the absence of long-lasting magma chambers beneath slow-spreading ridges (Perfit & Chadwick, 1998) inherently result from low extent of mantle melting (Langmuir et al., 1992; Perfit & Chadwick, 1998).

The thickness of the brittle lithosphere, defined by the 600°C isotherm (Abercrombie & Ekström, 2001; Mckenzie et al., 2005), varies locally, notably at the intersections between ridges and transform faults (TFs), called ridge-transform intersections (RTI) (Grevemeyer et al., 2019; Huang & Solomon, 1988; Phipps Morgan & Chen, 1993; Rundquist & Sobolev, 2002). Fox and Gallo (1984) first described the "cold edge effect" at RTIs, from the main observation of a deepening of the ridge axes near TFs. They showed that the RTI morphology is mostly controlled by the juxtaposition of an old, cold and thick lithosphere against the hot mantle, and the young and thin lithosphere of the spreading ridge axis. This contact causes a cooling of the mantle rising beneath the axis and a thickening of the axial lithosphere approaching the RTI. The main consequence of the "cold edge effect" is the decrease in the degree of partial melting, and thus in the volume of magma fed to the axis in the vicinity of the TF, resulting in the formation of a thinner crust. The lower magma supply generates temporary and isolated magma reservoirs, with less melt mixing, eventually leading to an increase of the variability in basalt composition compared to robust magmatic segments (Fox & Gallo, 1984; Langmuir & Bender, 1984; Phipps Morgan & Forsyth, 1988). Another proposed consequence of this effect is the welding of the young lithosphere with the adjacent, cold lithosphere, creating a shear couple between the two plates. This linkage causes the change in orientation of the minimum horizontal stress from normal to oblique to the spreading direction approaching the TF (Fox & Gallo, 1984).

The slow-spreading Mid-Atlantic Ridge (MAR) is offset by numerous TFs, especially in the equatorial zone between the latitudes of 5°N and 7°S which includes the large TF systems of Saint-Paul (~570 km cumulative offset), Romanche (~900 km offset) and Chain (~300 km offset) (Figure 1a). The Romanche TF offsets the MAR in a sinistral way resulting in a lithospheric age contrast of ~45 Ma.

Regardless of the cold-edge effect near TFs, the average temperature of the equatorial upper mantle has been shown to be colder than in adjacent regions. The axis of the equatorial MAR is deeper than in other MAR segments, reaching maximal depths of 4,000–5,000 m, compared to depths of ~3,000–4,000 m south of the Romanche TF (Anderson et al., 1973; Schilling et al., 1995). Lower degrees of melting relative to those observed along other MAR segments were estimated from peridotites and basalts collected in the equatorial MAR. The Romanche TF marks a boundary, with warmer estimated mantle temperatures at which decompression melting begins southward (Schilling et al., 1994, 1995). Furthermore, P- and S-wave tomographic models reveal the presence of a high-velocity zone (i.e., low temperature) in the upper mantle of the whole equatorial region (Dziewonski & Anderson, 1984; Zhang & Tanimoto, 1992). Recent studies based on seismic data have documented the presence of a slightly thinner-than-normal crust, 8–70 Ma-old, in the equatorial Atlantic Ocean (Marjanović et al., 2020; Wang & Singh, 2022).

The Romanche TF is one of the longest in the world, therefore, a strong cold-edge effect is expected (Bonatti et al., 1996; Ligi et al., 2005; Schilling et al., 1994, 1995). The eastern intersection of the Romanche TF with the MAR is influenced by the combination of the cold edge effect and the regional mantle temperature minimum under the equatorial Atlantic. Both effects decrease to the south with increasing distance from the TF. Previous studies on this Eastern Romanche Ridge-Transform Intersection (ERRTI) described an unusual ridge axis pattern with an oblique, en-echelon structure and a poorly defined NVZ within ~30 km of the ERRTI (Bonatti et al., 1996). These conditions of low melt production near the intersection appear to have been steady-state for a large part of the Romanche life span (more than 30 Ma; Bonatti et al., 2001; Gregory et al., 2021). However, the structure of the present-day NVZ was not described in detail by these authors and the impact of the thermal gradient on the mode of construction of the axial domain is poorly known. The aim of this study is to provide new constraints on the interplays between volcanic and tectonic activity through space and time under a transitional melt regime, from nearly amagmatic at the ridge-transform intersection toward a more magmatic one away from the TF.

To assess how volcanism and tectonics co-vary as a function of the distance to the TF, we interpreted bathymetric and backscatter data collected during the SMARTIES (Maia et al., 2019) and ILAB-SPARC (Singh, 2018) cruises. We augmented this interpretation with observations from manned Nautile submersible dives. The studied dives were performed during the SMARTIES cruise, and distributed along the NVZ from ~10 km south of the TF to ~80 km away from it (Figure 2). From these data we describe the axial structure, including the variations of

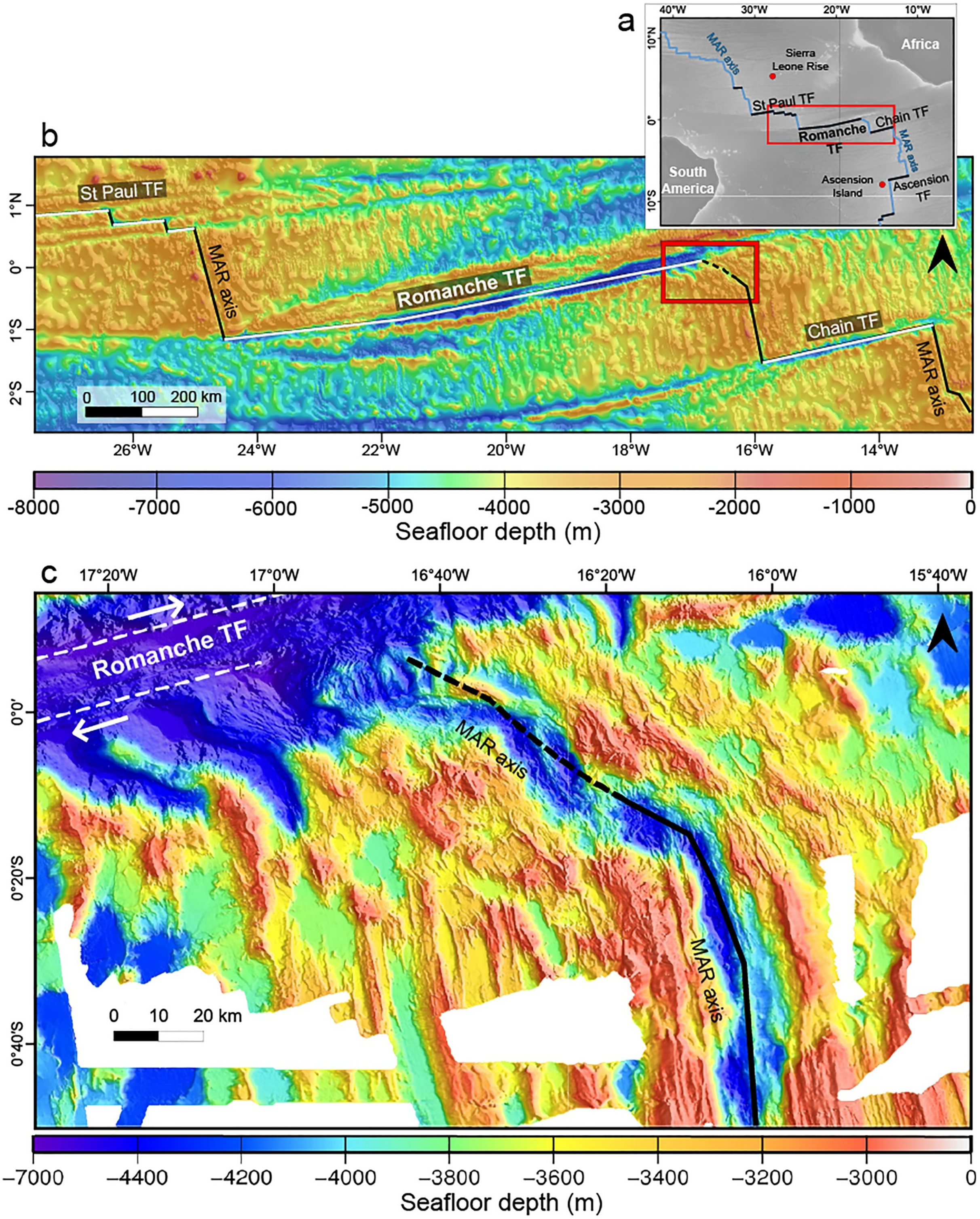

Figure 1. (a) Main transform faults (black lines) offsetting the equatorial Mid-Atlantic Ridge (blue line). The red box delimits the Equatorial Atlantic represented in (b) The red dots are hotspot locations from Basile et al. (2020) and Walowski et al. (2021). TF: Transform fault. Data source: GEBCO Compilation Group, 2022. The MAR axis represented in b and c, is based on Bonatti et al. (1996) interpretations. (b) Bathymetric map of the MAR axis between Saint-Paul and Chain transform faults. The MAR axis is marked by black solid and dashed lines and the transform fault systems by white lines. The red rectangle delimits the ERRTI (Eastern Romanche Ridge Transform Intersection) represented in (c) Data source: GEBCO Compilation Group, 2022. (c) Bathymetric map of the ERRTI, combining swath bathymetry collected during the SMARTIES cruise and previous cruises. The MAR axis is marked by black solid and dashed lines. Boundaries of the Romanche transform fault shear zone are highlighted by white dashed lines and the white arrows indicate the direction of relative plate motion.

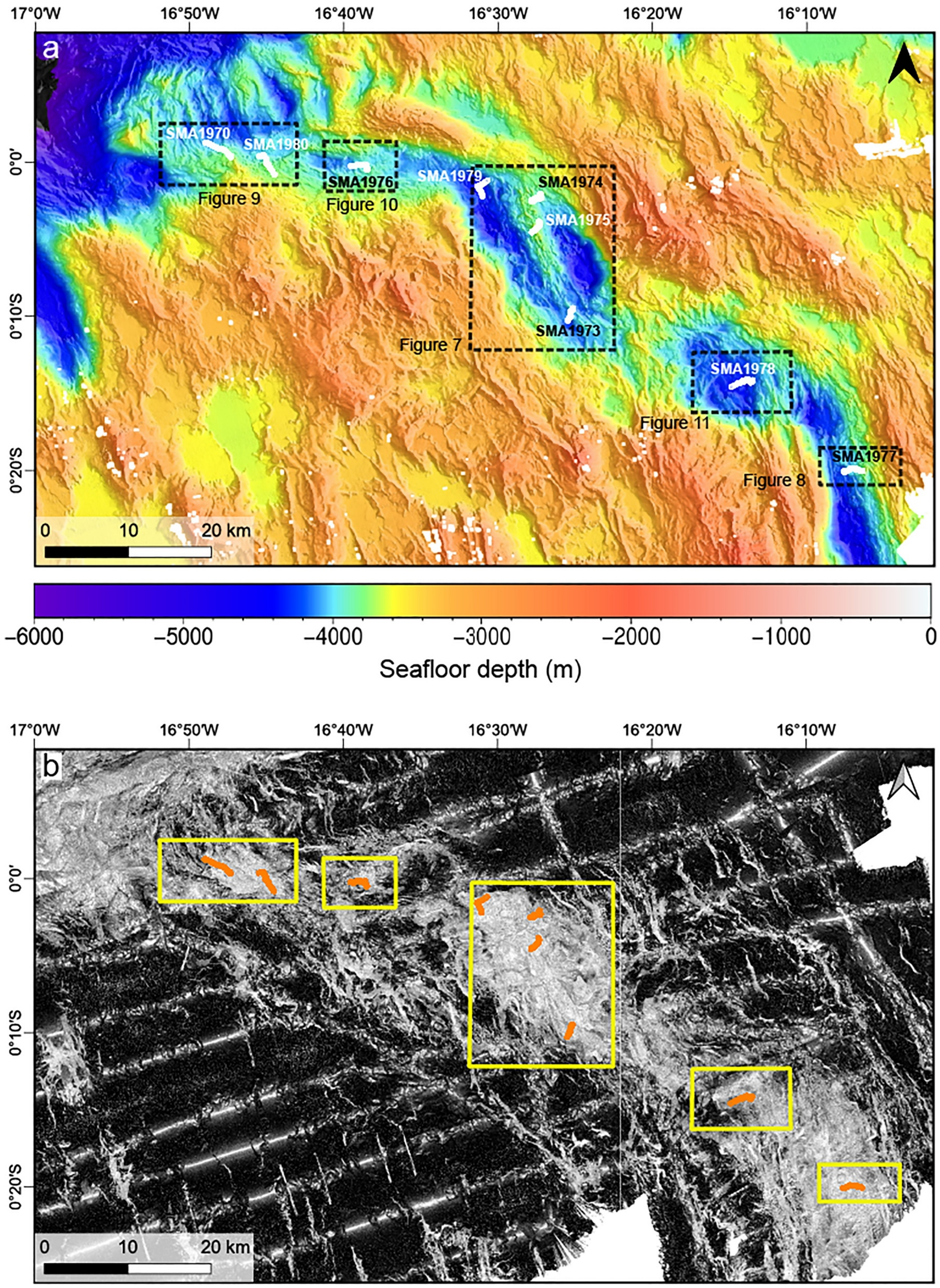

Figure 2. Bathymetry and backscatter of the neo-volcanic zone at the ERRTI. (a) Bathymetric map, combining swath bathymetry collected during the SMARTIES cruise and previous cruises. The white lines are the tracks of the dives analyzed in this study. The black dashed rectangles outline the mapped areas, where figure numbers correspond to the structural maps presented in the following sections. (b) Backscatter mosaic. High reflectivity intensity corresponds to light colors, and sedimented terrains with low backscatter intensity are dark. Dive tracks are shown in orange and mapped areas as yellow rectangles.

fault orientation along the axis. In order to have a first order approximation of the magma supply variations along axis, we used lava flow morphology as a proxy for the extrusion rate (Fink & Griffiths, 1992; Griffiths & Fink, 1992). We also report the size, shape of seamounts and their number per km^2 as another indication of the eruption dynamics and the amount of magma input (Cochran, 2008; Magde & Smith, 1995; Mendel & Sauter, 1997; Smith & Cann, 1992). Based on visual (dive videos) and echosounder (backscatter) estimation of sediment thickness, we determined a relative chronology of volcanic terrains, confirmed by absolute dating of four basaltic samples.

2. Geological Setting

The Romanche TF offsets the slow-spreading Mid-Atlantic Ridge near the equator (full spreading rate ~28 mm/yr, spreading direction N78°E in the study area; DeMets & Merkouriev, 2019). The section of the MAR located between the Romanche and Chain TF (segment eight in Schilling et al., 1994) is a ridge "super-segment", composed of segments separated by non-transform discontinuities (NTD) (Figure 1).

The southernmost segment, extending from the Chain TF to 0°15′S, has been described as a typical MAR segment displaying an active spreading center with recent volcanic constructions (Bonatti et al., 1996). Its northern part is shown in Figure 1c. The orientation of this segment is ~N160–170°E and its northern part shows directions ~N110–120E° (Bonatti et al., 1996). Harmon et al. (2018) also described this segment as an active spreading center associated with recent basalts and similar to those typically observed in the MAR. A second segment was identified by Bonatti et al. (1996), between 0°10′S and the equator, with an orientation of ~N160°E. According to these authors, the axial valley disappears 30 km south of the ridge-transform intersection, and the morphology of the ridge-transform intersection is poorly defined, since no deep active nodal basin or inside-corner high were identified. Bonatti et al. (1996) also reported the absence of a progressive deepening of the seafloor toward the TF, contrary to what was described near other Mid-Atlantic RTIs. Based on a limited number of dredged samples, the 30 km-wide band of seafloor south of the TF was interpreted to consist mostly of serpentinized mantle overlaid by a thin and discontinuous basaltic crust (Bonatti et al., 1996). The study of peridotites and basalts collected in the area suggested low degrees of melting, with predominantly amagmatic extension (Bonatti et al., 1993, 1996; Schilling et al., 1995). There is no clear geophysical evidence suggesting a present-day influence of hotspots on the MAR axis between the Romanche and Chain TF. However, according to Schilling et al. (1994) the mantle in the region from the Romanche to the Ascension TF (their segments 8–10) is characterized by an overall depleted composition, containing enriched mantle lumps. These fragments would result from a combined effect of a hotspot with delaminated subcontinental lithospheric mantle.

Ligi et al. (2005, 2008) developed numerical models of the mantle thermal structure and partial melting to estimate the extent of the cold edge effect for an offset similar to that of the Romanche TF. They compared their results with the composition of basalts collected along the MAR from ~220 km south of the Romanche TF to the ERRTI. The models suggest a strong decrease in the degree of mantle melting approaching the transform, with no partial melting within 30–40 km from the TF. This is consistent with the 30 km-wide band of outcropping serpentinized mantle described by Bonatti et al. (1996, 2001). The low magmatic production is also confirmed by Gregory et al. (2021) who estimated off-axis crustal thickness from seismic data. These authors highlighted that the crustal thickness, investigated ~60 km west of the ERRTI and ~100 km south to the TF, is variable (3.5–6 km), and thinner than that produced by magmatically robust segments of the MAR (7–9 km) (Canales et al., 2000; Dannowski et al., 2011; Hooft et al., 2000). The ERRTI was surveyed with a network of ocean-bottom seismometers (OBS) installed during the SMARTIES cruise. Velocity anomalies obtained from the OBS data show the presence of weakly serpentinized mantle in the RTI, supporting a tectonic dominated extension (Yu et al., 2023). Based on velocity anomalies, at the axis, from ~30 km south of the intersection, the accretion seems to be dominated by magmatism.

3. Data Acquisition and Analysis Methods

Two scales of observations, from shipborne data, and submersible, are combined to describe the structure of the ERRTI and the volcanic axis: segment and outcrop scales. We defined the general morphology of the axial ridge, identified the faults, fractures, volcanic edifices and described the lithologies. The sediment cover observed during dives and/or estimated as a function of the backscatter intensity is a proxy of relative ages of the seafloor (Cann & Smith, 2005; Lonsdale, 1978; Mitchell, 1993; Yeo et al., 2016).

3.1. Bathymetry and Backscatter Data

Bathymetric data were collected during the SMARTIES cruise (Maia et al., 2019) on board R/V *Pourquoi Pas?* with the multibeam echo sounder RESON 7150. Due to the expected depth range, including depths larger than 6,000 m, the frequency of 12 kHz was used, with 630 beams (1° × 1°) across a 120° opening, to optimize the cross-track sounding spacing (~5–15 m for seafloor depths of 2,000–6,000 m). The vertical depth resolution of the echosounder is ~10 m at these depths. The ship speed was 10 knt for most of the profiles. We adjusted it to 5 knt along the tracks in planned submersible dive areas, thus decreasing the along-track spacing between sounding pings from ~100 to ~50 m, and collected several overlaying bathymetric swaths, to ensure an improved density of depth measurements in these areas. The bathymetric data was processed with the Globe software (IFREMER) and combined with bathymetry data acquired during the ILAB-SPARC cruise with the same echosounder (Singh, 2018). These data were used to create grids of the ERRTI and the MAR axis south of it with a grid step down to 20 m (Figure 2a). However, for 20 and 30 m grids stripes visible in the maps, they appear where interpolation between measurements was necessary. These stripes are local artifacts and were not interpreted as structures. For the figures presented in this article, we used the 50 m grids, which do not show these artifacts but present smoother bathymetry.

Backscatter data were corrected for the incidence angle dependence related to the antennas directivity pattern and compiled into mosaics down to 10 m grid spacing with SonarScope software (IFREMER). Reflectivity intensity depends on the incidence angle (topography), the surface roughness (micro-topography) and the nature of the seafloor (sediments, lava flows, or scree) (Jackson et al., 1986; Lurton et al., 2015). Considering the topography, we used the backscatter intensity as a proxy for the sediment thickness, and thus for the relative age of the terrain. In our mosaics, high backscattering is shown in light gray, while low backscattering is shown in dark gray (Figure 2b).

3.2. Submersible Videos and Pictures

During the SMARTIES cruise, 25 dives were carried out with the human operated vehicle (HOV) Nautile from the French Oceanographic Fleet. Nine dives explored axial volcanic areas from 10 km to about 80 km south to the Romanche TF (Figure 2). During the dives, videos were recorded with a fixed and a mobile camera and photographs were automatically taken every 10 seconds. We corrected the dive navigation files, analyzed the videos, and logged the main observations for the nine dives with the Adélie Vidéo software developed by IFREMER (Text S1 in Supporting Information S1). Basalt samples were also collected during the dives and their glass composition was studied by Verhoest (2022).

3.3. Volcano-Tectonic Mapping

We produced structural maps of the segments and discontinuities from bathymetric and backscatter maps, and geological maps for each dive from outcrop observations (Figures S6–S14 and Text S3–S11 in Supporting Information S1). Combining these two observation scales, we were able to describe the general structure of the NVZ as a function of the distance from the Romanche TF, as well as variations of the size and shape of volcanic edifices.

3.3.1. Observations at the Segment Scale

Volcanic features and faults were identified from bathymetric maps and backscatter mosaics and drawn using the Global Mapper software (Figure S1 in Supporting Information S1). These observations were then transferred to a QGIS software project to build the geological maps. We defined four categories of volcanic constructions: volcanoes, hummocky areas, terraces and ridges (Figure S2 and Text S2 in Supporting Information S1). Volcanoes have been categorized as cones or seamounts, according to their size, where seamounts have a diameter >500 m and a height >50 m (Searle et al., 2010; Smith et al., 1995).

We interpreted linear escarpments from 10 m to more than 300 m high as steeply-dipping normal faults. The active or recently active faults have talus consisting of blocks free of sediments, whose rough surfaces appear as streaked zones on backscatter maps (Figure S3 in Supporting Information S1).

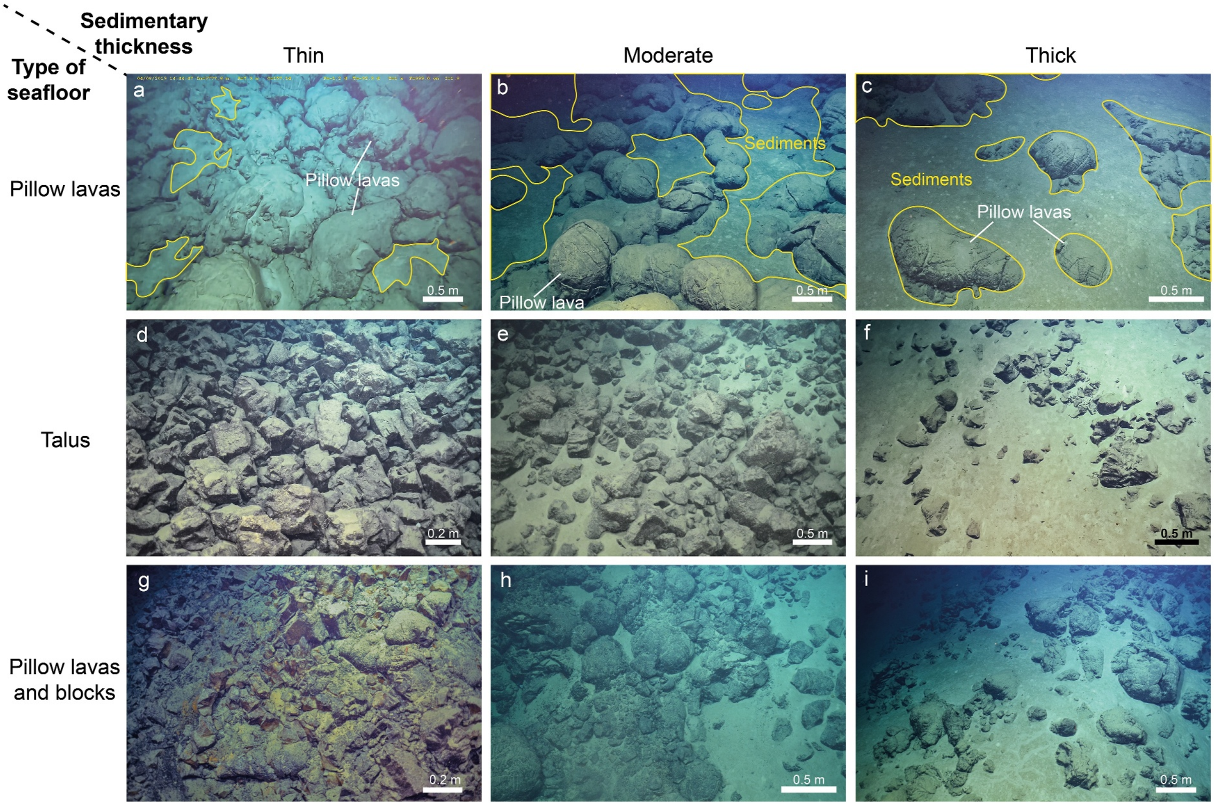

Figure 3. Photographs of the main types of seafloors (pillow lavas, talus and "pillow lavas and blocks") observed with various sedimentary thicknesses. The "thin cover" corresponds to an almost total absence or to a light layer of sediments on pillows or blocks and small sediment pockets observed between pillows or blocks. A "moderate cover" is defined as a thicker sediment layer, with connected pockets, although pillows and blocks are still visible. A thick sediment blanket characterizes the "thick cover", where only the top of rounded pillows is still visible, and few blocks appear between sediment ponds. On pictures a, b and c the contacts between sediment and pillow lavas are outlined by yellow lines.

Detachment faults are long-lived normal faults whose rotated, smooth surface becomes nearly horizontal or domed away from the axis, sometimes presenting corrugations parallel to the spreading direction (Cann et al., 1997; Escartín et al., 2003).

3.3.2. Observations at the Outcrop Scale

Based on submersible observations, the seafloor geology was divided into four main categories, namely: pillow lavas, talus, "pillow lavas and blocks" and sediments (Figure 3). The "pillow lavas and blocks" correspond to areas where pillow lavas and fragments of broken pillows are present in the same proportions.

Some massive flows were observed in fault scarps, interbedded with pillows. They appear as continuous layers, tens of centimeters to two m thick, which are characterized by massive facies with columnar jointing at the base and top of the layers (Figure 4a). These outcrops are too small to be considered a main category. Peridotite and gabbro or breccia outcrops have been described only in dive SMA1976 (Figures 2 and 4b-c). Pillow lavas, talus, "pillow lavas and blocks" were further distinguished according to three levels of sedimentary cover (Figure 3): thin, moderate and thick (Colman et al., 2012; Fox et al., 1988; Yeo & Searle, 2013). This classification allows us to compare the sediment thickness within and between dives from a same zone. When pillows were barely discernible and blocks sparsely present, the seafloor was considered "fully sedimented".

The observed sediment thickness is used as a proxy to define the relative seafloor age. An average sedimentation rate of 5 mm/ka for areas younger than 10 Ma was estimated in the segment close to Chain TF from the sediment thickness measured on seismic profiles (Agius et al., 2018). Based on this estimation, the "thin cover" sedimentation should correspond to a seafloor age between 0 and ~40 ka, the "moderate cover" to ages between ~40 and 100 ka and the "thick cover" corresponds to ages between ~100 and 150 ka. The topography of the seafloor

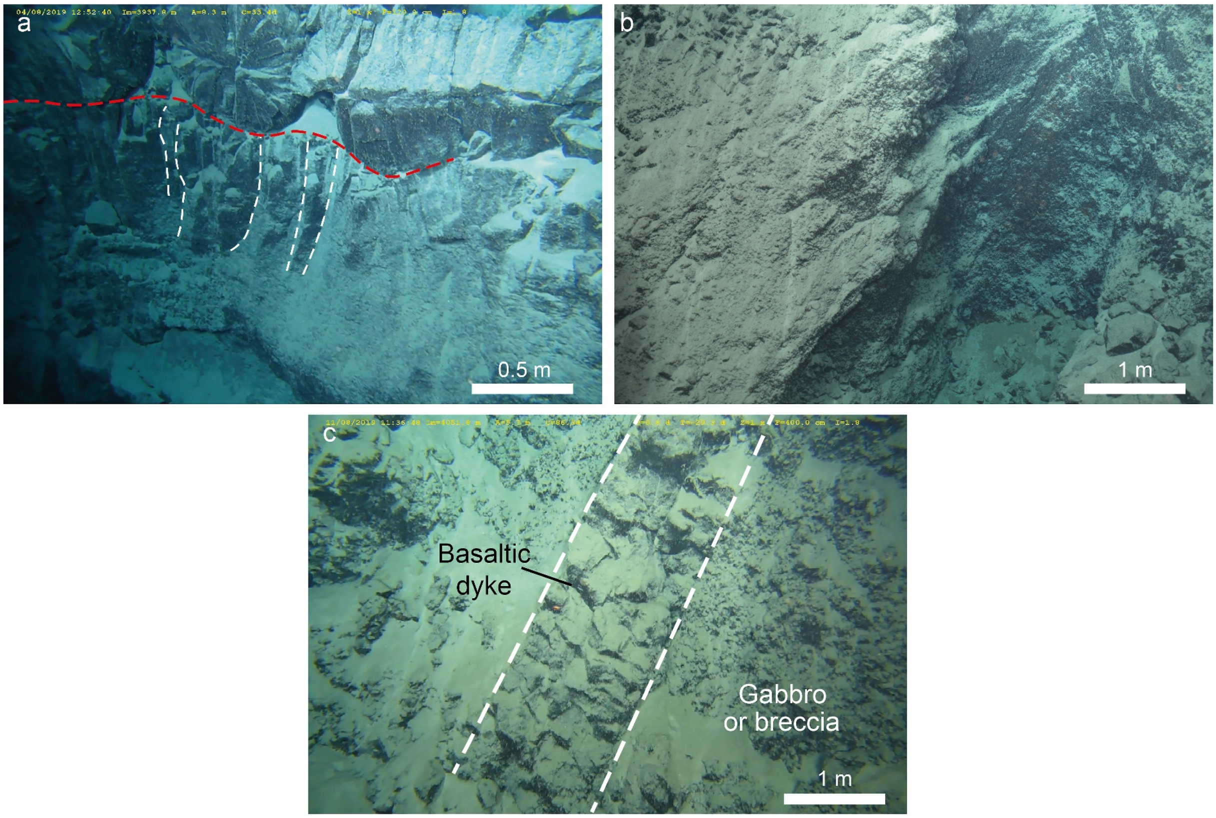

Figure 4. Photographs taken during HOV dives. (a) Sheet flow layer (under the red dashed line) overlaid by pillows. The white dashed lines delimit the columnar joints (dive SMA1970). (b) massive peridotite exposed in a fault scarp. (c) Gabbro or breccia with a granular texture cut by a basaltic dike (delimited by dashed lines).

was taken into account, as sediments tend to accumulate at the base of slopes or on flat terrain rather than on steep slopes. The intensity and the direction of near-bottom currents can also locally influence the sediment thickness. However, over most of the area, we observed no ripples or drifts in sediments that could indicate that their deposition was strongly affected by currents, which supports the use of sediment cover as a proxy of relative seafloor age. Some of the volcano summits were devoid of sediments, either because the volcanic activity was recent or because of the localized effect of currents. In the first case, the glassy surface of the pillow was visible (Figure S4 in Supporting Information S1).

Lava flow morphologies were carefully described because they can be used as proxies to estimate eruption dynamics along an AVR. Laboratory experiments suggest that lava flow morphology is controlled by the balance between the rate of cooling and the rate of extrusion of the lava (Fink & Griffiths, 1992; Griffiths & Fink, 1992). Pillow lavas tend to form at lower eruption rates and higher viscosity, while sheet and lobate flows require higher extrusion rates (Gregg & Fink, 1995).

Faults and fissures are present all over the study area (Figures 5a and 5b). We also used sediment thickness as a proxy to estimate the relative age of exhumation of tectonic structures. Fissures filled by blocks covered only by a thin sediment layer were interpreted to be recent features. If they were covered by a thicker sediment layer, they were considered older.

The fault scarps were considered old if they were slightly or moderately covered by sediments and exposed pillow sections covered by a manganese crust (Figure 5c), while younger fault scarps were free of sediments, and exposed broken pillows coated by iron hydroxides characterized by an orange patina, and glass shards accumulations between pillows (Figure 5d). As the iron hydroxide coating develops quickly after basalt exposition to seawater (Alt et al., 1986; Honnorez et al., 1978; Pichler et al., 1999), this alteration suggests a recent fault activity. Few grabens were observed, and their central block was always covered by sediments.

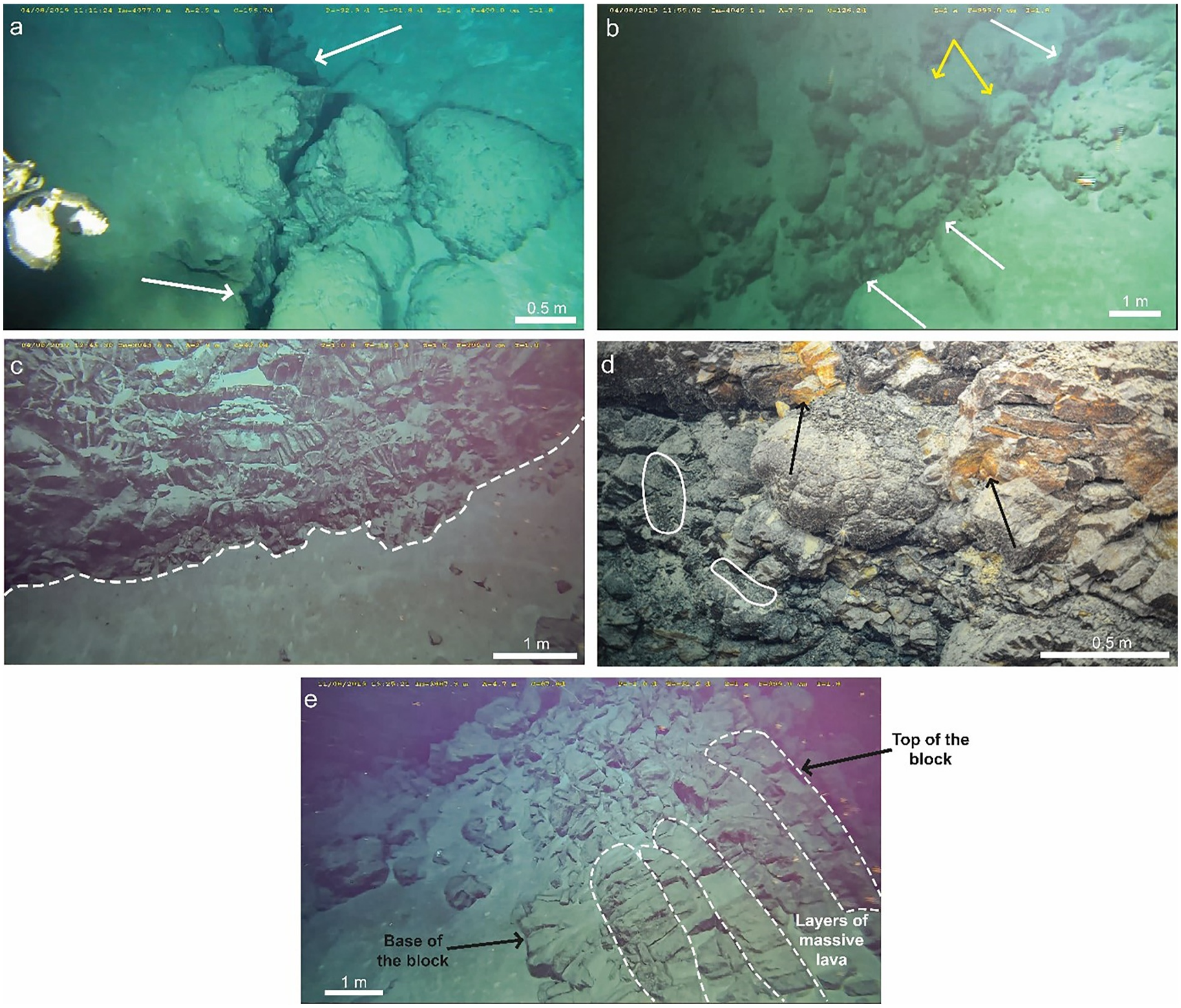

Figure 5. Photographs taken during HOV dives showing examples of observed structural features. (a) Thin fissure cutting pillows (white arrows), (b) large fissure (white arrows) cutting pillows and partly covered by more recent pillows (yellow arrows), (c) fault scarp moderately covered by sediments, exposing the radial fracturation of pillows, the foot of the scarp (delimited by the dashed line) is fully sedimented, (d) fault scarp without sediment, exposing sections of pillows coated by orange iron hydroxide (black arrows); accumulation of glass shards are present between pillows (white lines), (e) sheet flows tilted ∼90° (white dashed lines) and pillows.

3.4. Geological Maps

We compiled observations into morpho-structural maps where we distinguish five different relative volcanic ages based on the intensity of the backscatter and the sediment thickness observed during the dives. The five types of volcanic seafloor are defined as: very recent (highest backscatter intensity), recent, sub-recent, sub-old, and old volcanism (lowest backscatter intensity) (Figure S5 in Supporting Information S1). The classification of relative volcanic age is common to all mapped zones. Maps also include sedimented areas, talus zones, fault scarps, and detachment surfaces.

3.5. Volcanic Shape Measurements

We measured the base and summit diameters, height, and volume of individual volcanoes. The height-to-basal diameter ratio and the flatness were hence used as proxies for the average eruption rate, while the size of edifices and density of seamounts were used to infer the magma supply (Cochran, 2008; Magde & Smith, 1995; Mendel & Sauter, 1997; Smith & Cann, 1992).

The morphological parameters and volume of volcanic edifices identified on bathymetric grids were measured with Global Mapper software tools. Two perpendicular profiles were traced on each volcano. Edifice height, top and base diameters were measured and the values from both profiles were averaged. All edifices with a height <20 m were considered too close to the vertical depth grid spacing and were not included in the analyses. The shape of an edifice is defined based on two parameters: the height-to-basal diameter ratio and the flatness (diameter top/basal diameter). The boundaries of edifices were used to obtain their volume (Geissler et al., 2020). We estimated the seamount density by dividing the number of volcanoes identified as seamount by the surface of the segments and NTDs containing seamounts.

3.6. Geochronology: Selection Criteria and Sample Preparation

To provide more quantitative constraints on the volcanic activity, we selected four samples for dating. ^{40}Ar/^{39}Ar dating of mid-ocean ridge basalts (MORB) is challenging (Guillou et al., 2017) because several factors limit the effectiveness and reliability of the K-Ar radiometric clock (i.e., the low K contents of MORB, the small decay constant of ^{40}K, the likely retention of mantle-derived non-atmospheric ^{40}Ar, as well as low- and/or high-temperature alteration). Nevertheless, several studies (Duncan & Hogan, 1994; Guillou et al., 2017; Jicha et al., 2012; Jourdan et al., 2012; Sharp & Renne, 2005; Turrin et al., 2008) have demonstrated that the dating of low radiogenic ^{40}Ar (^{40}Ar*) samples is no longer out of reach. Small amounts of ^{40}Ar* can be accurately resolved from the predominantly atmospheric ^{40}Ar in young and weakly potassic samples.

During the sample selection, glassy samples were avoided because they possibly bear argon excess caused by rapid quenching under high hydrostatic pressure conditions. Accordingly, we selected sample pieces at least 4 cm away from the glassy rims of the pillow lavas. Another concern is partial alteration by seawater and hydrothermal activity that may result in gain or leaching of K with dramatic effects on the reliability of the derived K-Ar ages. We have used major element analyses to estimate the degree of alteration (Table S1, Text S12 in Supporting Information S1). The loss-on-ignition (L.O.I.) values of the four selected samples range from −0.43% to 0.97%. We also used the alteration index (A.I.) of Baksi (2007) which is based on ^{36}Ar contents to evaluate the freshness of the samples (Text S13 in Supporting Information S1). The last parameter to consider is the K content of the sample, since the method is based on the disintegration of ^{40}K to ^{40}Ar. MORBs usually range very low in K (<0.2 wt%). However, the relatively high-K contents of the four dated samples (0.41–1.46 wt%; Table S1 in Supporting Information S1), improve the quality of the experimental conditions, because the rocks are expected to have developed a greater amount of ^{40}Ar*.

After macroscopic and microscopic examinations, groundmass from fresh samples was prepared following the method of Guillou et al. (2017). The samples were crushed and sieved to 125–250 μm size fractions and ultrasonically washed in acetic acid (1N) during 1-hr at a temperature of 60°C, to remove any secondary mineral phases. Phenocrysts and xenocrysts are potential carriers of extraneous ^{40}Ar (including excess and inherited components), hence in the 125–250 μm size fraction, phenocrysts, fragments with phenocrysts and possible fragments containing secondary mineral phases were eliminated using magnetic separation and visual hand-picking under a binocular. Phenocrysts are distinguished from the groundmass fragments by their lighter color and their shinier appearance. The mass-spectrometric measurements protocol is described in Text S14 in Supporting Information S1.

4. Results

4.1. Structure of the Super-Segment Between the Romanche and Chain Transform Faults

We have re-interpreted the structure of the super-segment between Romanche and Chain TFs to be composed of four second-order ridge segments, separated by non-transform ridge axis discontinuities (NTD), offsetting the segments by ~5–35 km. We have named those segments RC1 to RC4 (RC for Romanche to Chain), from north to south (Figure 6a). The SMARTIES cruise thoroughly explored the eastern part of the Romanche TF and the adjacent first two Mid-Atlantic Ridge segments southwards as well as the northern portion of the third segment (RC3). The segment RC4 was studied by Harmon et al. (2018).

The first segment RC1 (~20 km long) abuts the TF valley. The north-western part of the segment is delimited by a deep, heavily sedimented nodal basin. Its eastern part consists of a large oceanic core complex (OCC), which extends to the eastern flank in a faulted dome (Figure 6b; Maia et al., 2019, 2020). The segment RC1 presents no clear trace of recent volcanic activity such as volcanic edifices or fresh basalts (Bonatti et al., 1996; Maia et al., 2019). The NTD1 is a ~35 km, left-stepping offset roughly oriented N76°E. Most faults affecting the

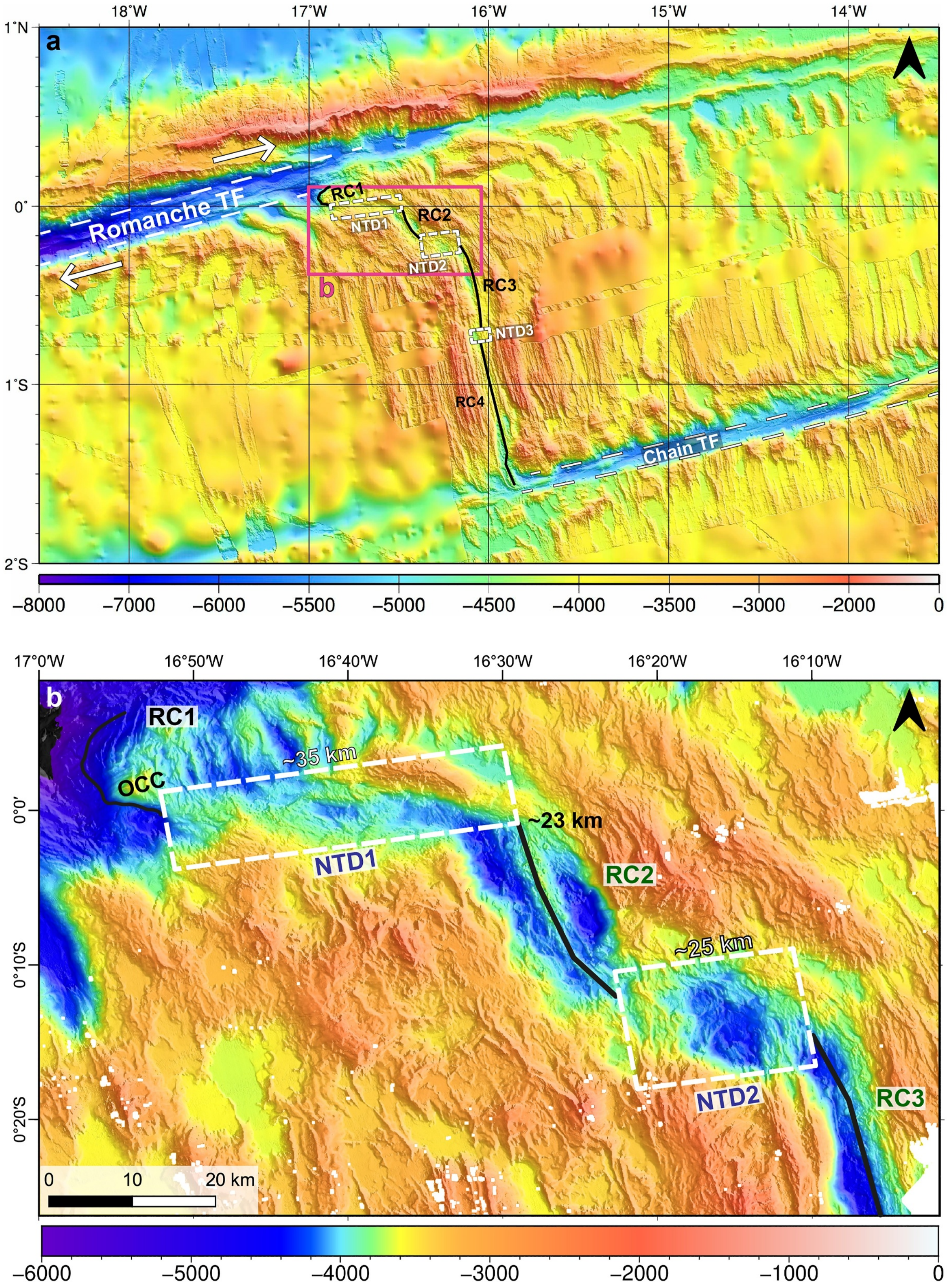

Figure 6. (a) Bathymetric map of the MAR super-segment between Romanche and Chain transform faults. The MAR axis is structured into four segments RC 1 to 4, offset by three non-transform discontinuities (NTD 1 to 3). The ridge axis is represented by thick black lines and discontinuities by the white boxes. Boundaries of the transform fault shear zone are highlighted by white dotted lines and the white arrows indicate the direction of plate motion. (b) Bathymetric map of the MAR axis at the ERRTI, from RC1 to the northern part of RC3.

discontinuity are normal faults, oblique to the spreading direction. The NTD is delimited at its northeast part by a peridotite hill trending ~N105°E and at its southern part by a gentle slope (Figure 6b). Segment RC2, ~23 km long, has its northern tip located ~30 km south of the Romanche TF, and has a well-defined axial valley oriented ~ N150°E. There is a robust AVR at its center, composed of numerous volcanic edifices and standing out up to ~520 m above the valley floor. RC2 is the first volcanic segment away from the TF. The NTD2 offsets the segments RC2 and RC3 by ~25 km and includes a deep oblique basin. The segment RC3 is 50 km long and orthogonal to the spreading direction. The magmatic segments RC3 and RC4 are offset by a small NTD (Figure 6a).

Our study is focused on the volcano-tectonic characteristics of the axial domain, explored during the SMARTIES cruise, from NTD1 to the northern part of RC3, forming a ~120 km long section of the MAR south of the ERRTI (Figure 6b). As no clear volcanic feature was observed in RC1, it will not be discussed in this paper. In the following sections, we summarize the observations, resulting from the analysis of submersible videos, bathymetry and backscatter maps, made in the volcanic segments, then in the discontinuities, the morphology of seamounts and the ages obtained on the four samples.

4.2. Segment RC2

The axial domain of segment RC2 corresponds to a valley delimited by large normal faults, with a robust volcanic ridge in the center (Figure 7). The axial valley is bounded to the east by N120–140°E-trending normal faults and to the west by N120 to N170°E-trending normal faults cut by gullies with talus.

The northern section of the main volcanic ridge is ~12 km wide and oriented N150°E, while its southern part is narrower (~5 km) and trends N130°E. The height of the AVR above the valley floor decreases from north to south (520–270 m, respectively). This ridge comprises elongated ridges, small cones, seamounts and terraces (Figure 7). On the east side of the valley, volcanic edifice alignments and faults affecting the axial valley trend N130–150°E, whereas to the west, the main ridge, the volcanic structures and the faults trend N160°E (Figure 7). In the eastern and southern parts of the valley, the reflectivity intensity is low, suggesting a thicker sedimentary cover. On the contrary, the presence of some patches of high backscatter intensity on the northwestern side of the valley suggests more recent volcanic activity (Figures 7d and 7e). The segment shows more recent and more robust volcanic constructions on the north and west of the axial valley.

Pillow lavas dominate the volcanic morphology, with rare sheet flows only visible within some fault scarps (Figures S6-9 and Texts S3-6 in Supporting Information S1). The northwestern and northeastern parts of the ridge were explored during dives SMA1979 (16°31′W, 0°01′S; Figure S6 in Supporting Information S1) and SMA1974 (16°27′W, 0°02′S; Figure S7 in Supporting Information S1), respectively. The central portion of the ridge was surveyed during dive SMA1975 (16°27′W, 0°04′S; Figure S8 in Supporting Information S1) and its southern part during dive SMA1973 (16°25′W, 0°09′S; Figure S9 in Supporting Information S1). From dive descriptions, the eastern and southern parts of the segment appear to be covered by thicker sediments than the northern and central parts, confirming the backscatter observations (Figures 7d and 7e). The presence of iron hydroxide and glass shards on some fault scarps explored during dives SMA1979 and SMA1975 suggest that the tectonic activity is recent (cf. Section 3.3.2, § 4). Along the dive paths, the faults and fractures have orientations varying between N120 and 150°E. Along dives SMA1979 and SMA1973, located near the segment tips, some faults have an east-west direction (Figure 7c, and Figures S6 and S9 in Supporting Information S1).

4.3. Segment RC3

The northern part of segment RC3 displays an asymmetric axial valley. It is bounded to the west by a detachment fault with possibly a talus at its base, while the eastern side is affected by a series of N170°E-trending, inward-facing normal faults (Figures 6 and 8). The western side of the axial valley is deeper than the eastern one.

Elongated ridges, cones, hummocky terrains, seamounts and terraces constitute the neo-volcanic ridge (Figures 8a and 8b). Some parts of the seafloor are smooth, without visible edifices, and are possibly covered by lava flows. The backscatter intensity suggests that the western part of the valley floor is slightly younger than the eastern portion, an observation which was confirmed during the dive SMA1977 (16°6.9′W, 0°20.0′S) (Figures 8d and 8e and Figure S10 in Supporting Information S1). Poorly-sedimented pillow lavas were observed during the dive, with only one thin sheet flow exposed in a fault scarp. The tectonic activity appears to be recent, with numerous

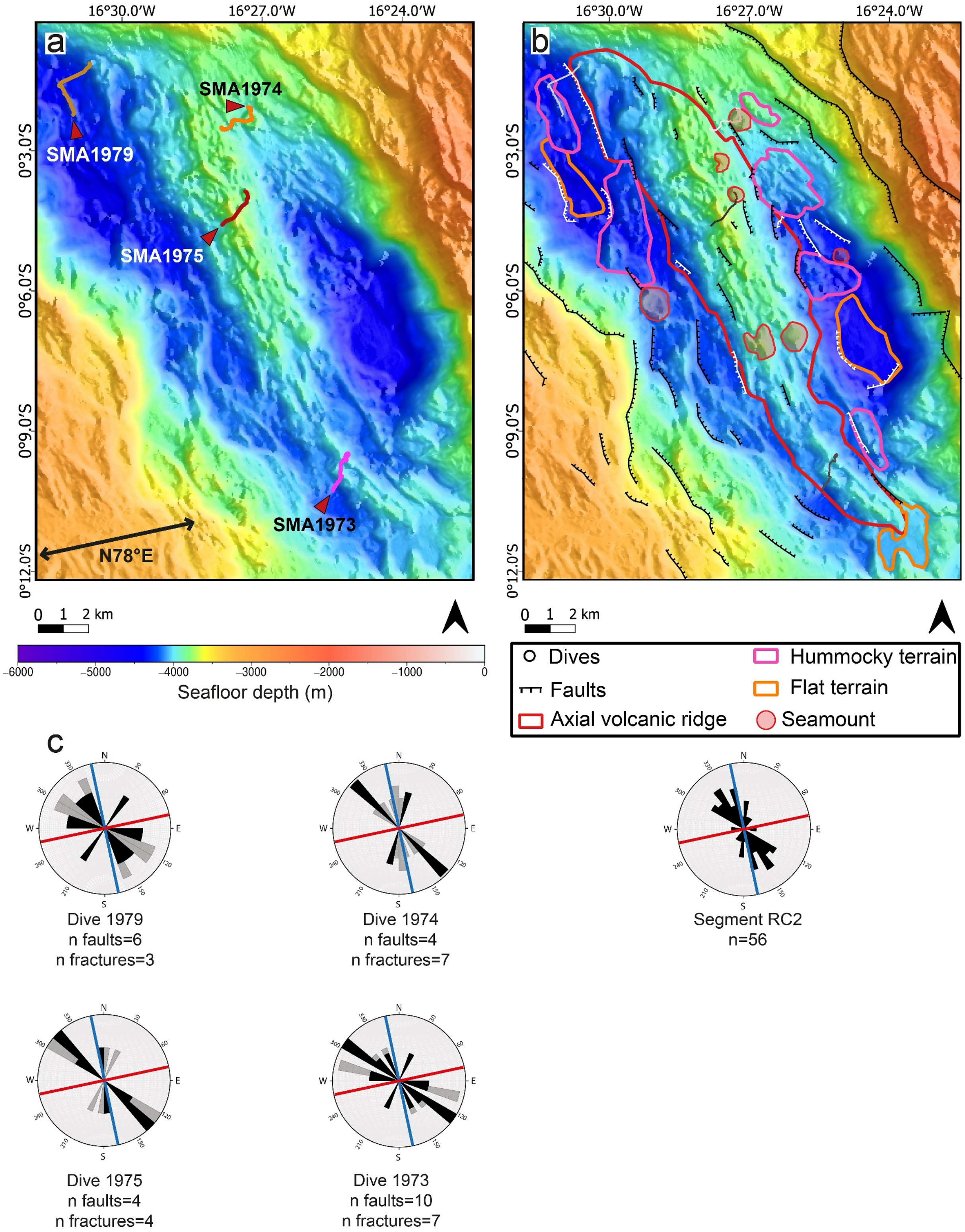

Figure 7. Multibeam bathymetry (a) and (b) and rose diagrams (c) of segment RC2. Location in Figure 2. (a) Bathymetric map including the tracks of the dives SMA1979, SMA1974, SMA1975 and SMA1973. The double arrow indicates the spreading direction. (b) Main volcano-tectonic features reported on the bathymetric map including axial volcanic ridge (red line), hummocky (pink line) and flat (orange line) volcanic terrains, seamounts (brownish surfaces) and faults. (c) Rose diagrams of fault and fissure orientations for each dive (left) and at regional scale (right). Fault orientations are in black, fissures in light gray, n is the number of faults or fractures. The red line represents the spreading direction (DeMets & Merkouriev, 2019) and the blue line the direction normal to spreading. (d) Backscatter mosaic shown with high intensity with light tones. (e) Structural map of segment RC2.

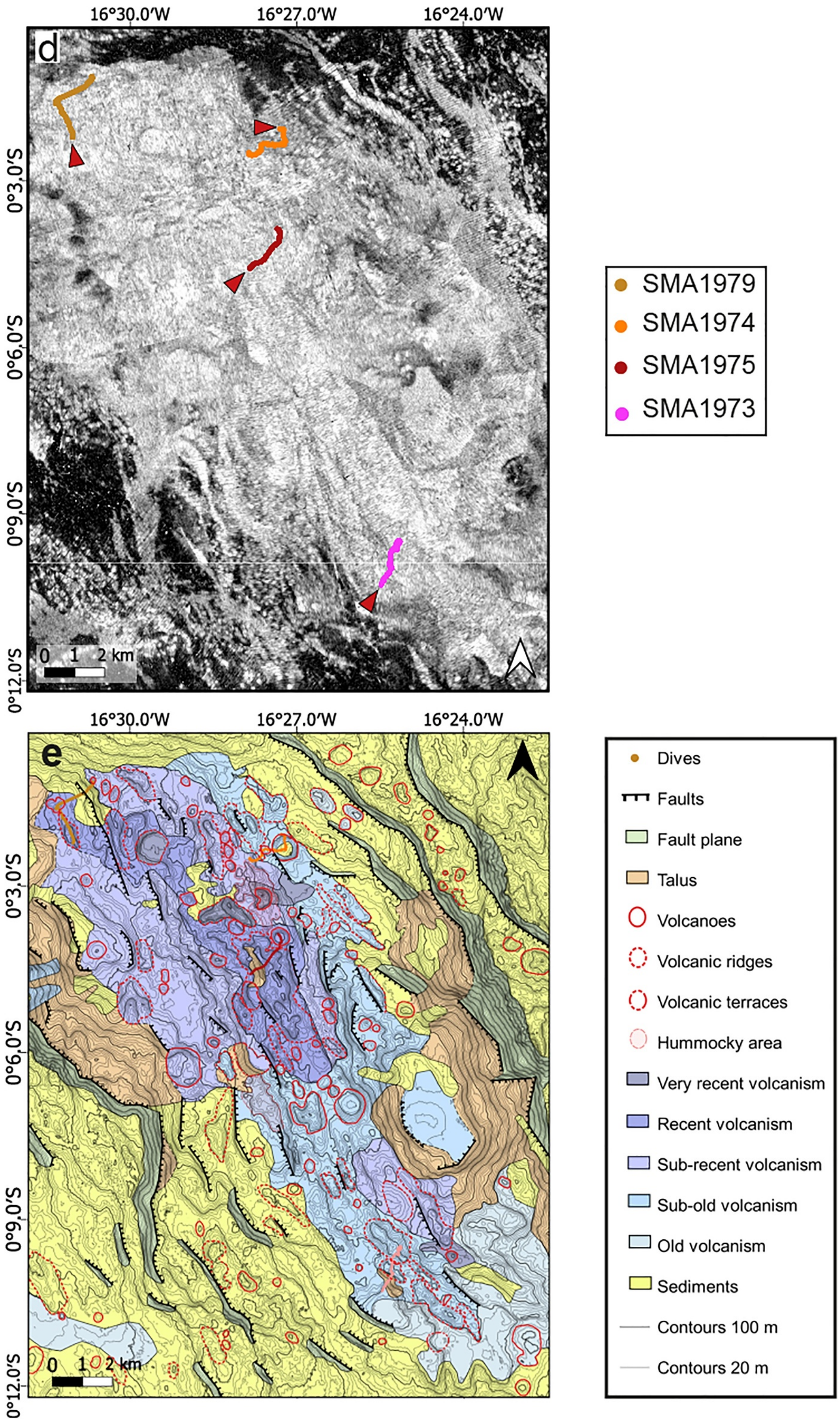

Figure 7. (Continued)

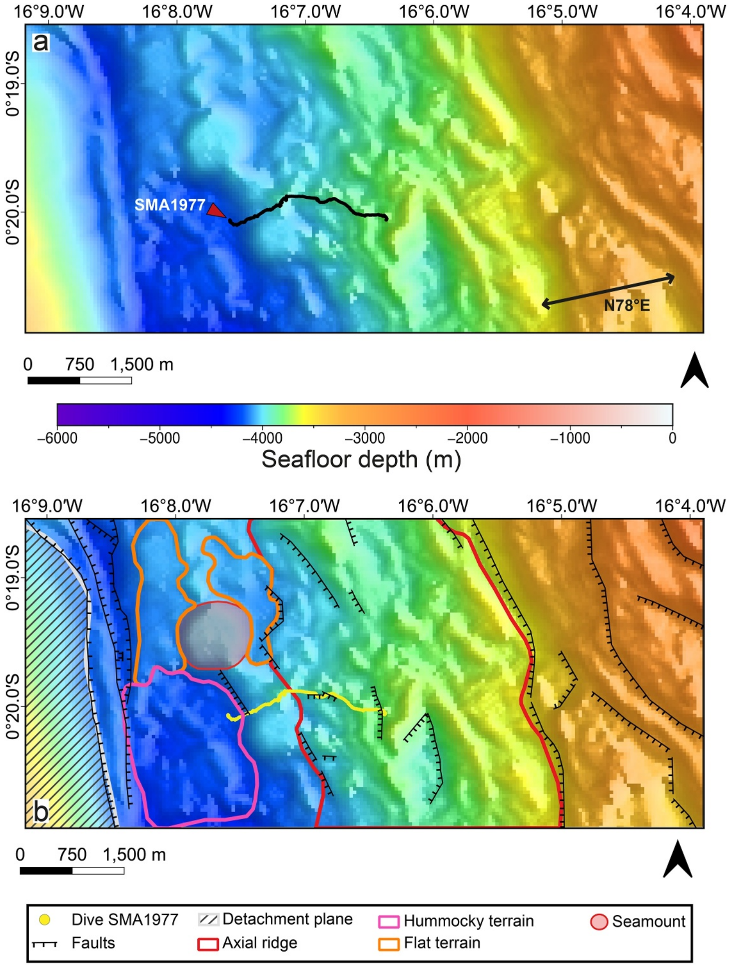

Figure 8. Multibeam bathymetry (a) and (b) and rose diagrams (c) of the northern part of the segment RC3. (b) The hatched area represents the detachment surface. (c) Rose diagrams of fault orientations along the path of the dive (top) and at regional scale (bottom), n is number of faults. Faults, red and blue lines, as in this figure. (d) Backscatter mosaic with high intensity shown in light tones. (e) Structural map of the northern part of the segment RC3.

fault scarps coated by iron hydroxide and displaying fresh broken up glass shards (cf. Section 3.3.2, § 4). In addition, tectonic and volcanic events appear to alternate over a short period as attested by pillows locally flowing over the fault scarps from the summit of the volcanoes. The faults have two main orientations, one ~ east-west, as described in dives near the segment RC2 tips, and the other 160–180°E (Figure 8c).

4.4. Non-Transform Discontinuity 1

The NTD1 (16°51.6′W–16°31.2′W) is a transtensive discontinuity marking the boundary between the segments RC1 and RC2. The NTD is affected by normal faults trending east-west to N120–140°E (Figures 9c–10c). This discontinuity hosts the first volcanic edifices away from the ERRTI, with four clusters of volcanoes and some rare narrow ridges, aligned in two directions, N90°–110°E and N140–150°E (Figures 9 and 10).

The dives explored three volcanic clusters, two in the western part of NTD1 (Figure 9): dive SMA1970 (16°48.59′W–16°47.19′W; Figure S11 in Supporting Information S1) and dive SMA1980 (16°45.29′W-16°44.28′W; Figure S12 in Supporting Information S1), and one in the eastern part of the discontinuity (dive SMA1976, 16°39.33′W–16°38.26′W, Figure 10 and Figure S13 in Supporting Information S1). Pillow lava flows dominate the landscape, although in the cross sections provided by the fault scarps a few thin sheet flows are observed between pillow lava layers (dive SMA1970, Figure 4a), and at the summit of two cones (dive SMA1976, Figure 5e). The volcanic activity seems to be more recent in the shallow parts at the end of the dives SMA1970 and SMA1976

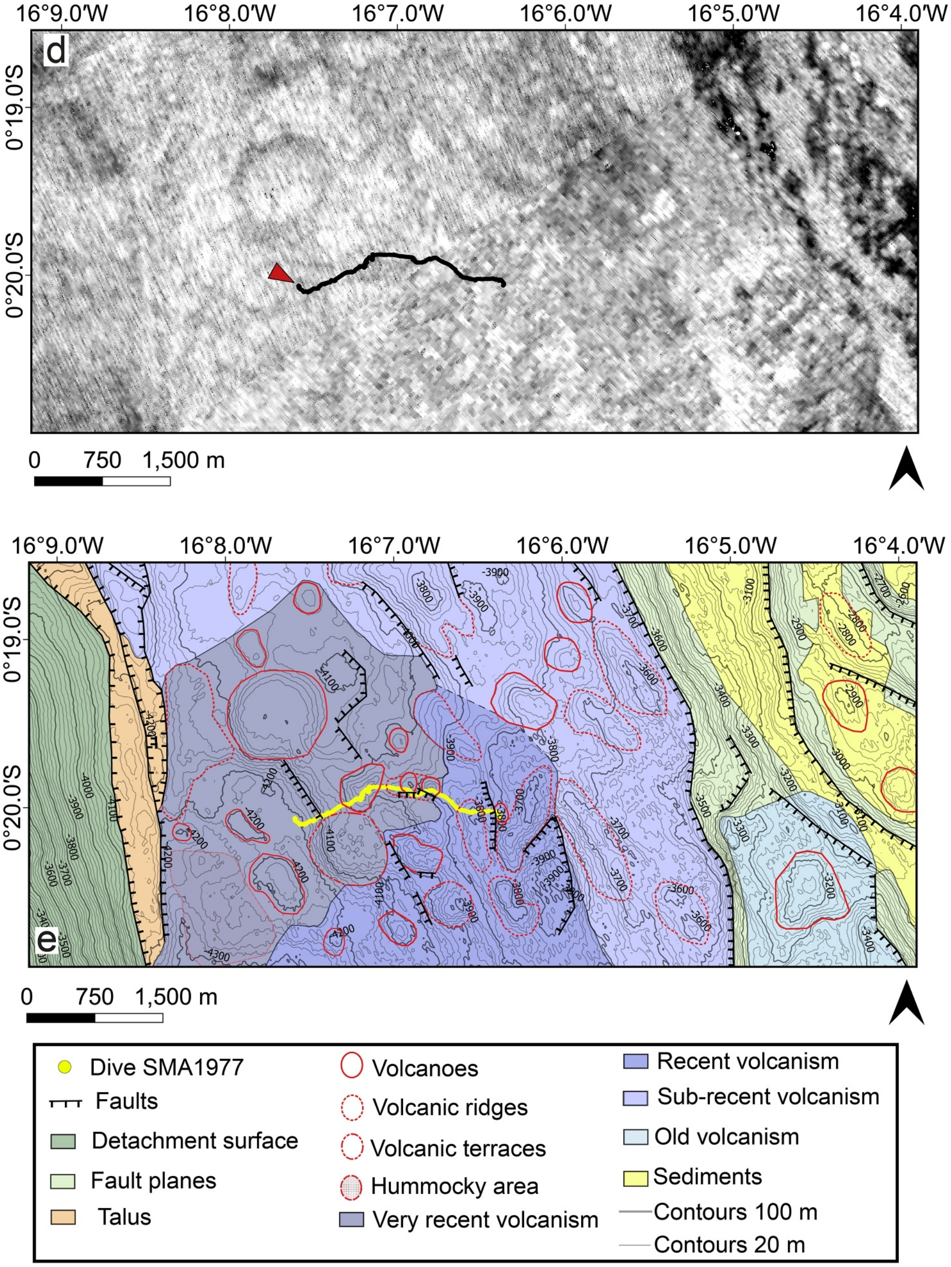

Figure 8. (Continued)

(Figures 9d and 9e and 10c and 10d). During the dive SMA1976, peridotite and gabbro or breccia were recognized in a fault scarp (Figures 4b and 4c). This is the only direct observation of ultramafic rocks on the floor of the inner axial domain in our study area. The thin sediment cover observed on some fault scarps and fractures suggests relatively recent tectonic activity. In the western part of NTD1, the faults and fractures have mainly N110–140°E orientations (Figure 9c). Some N130–170°E-trending faults are observed at the end of the dive SMA1970 (Figure 9c). In the eastern part of the discontinuity, faults have mainly N80–110°E orientations (Figure 10e). Along the track of dive SMA1976, two families of secondary faults are present, one with N120–150°E orientations and the other with N160–195°E orientations.

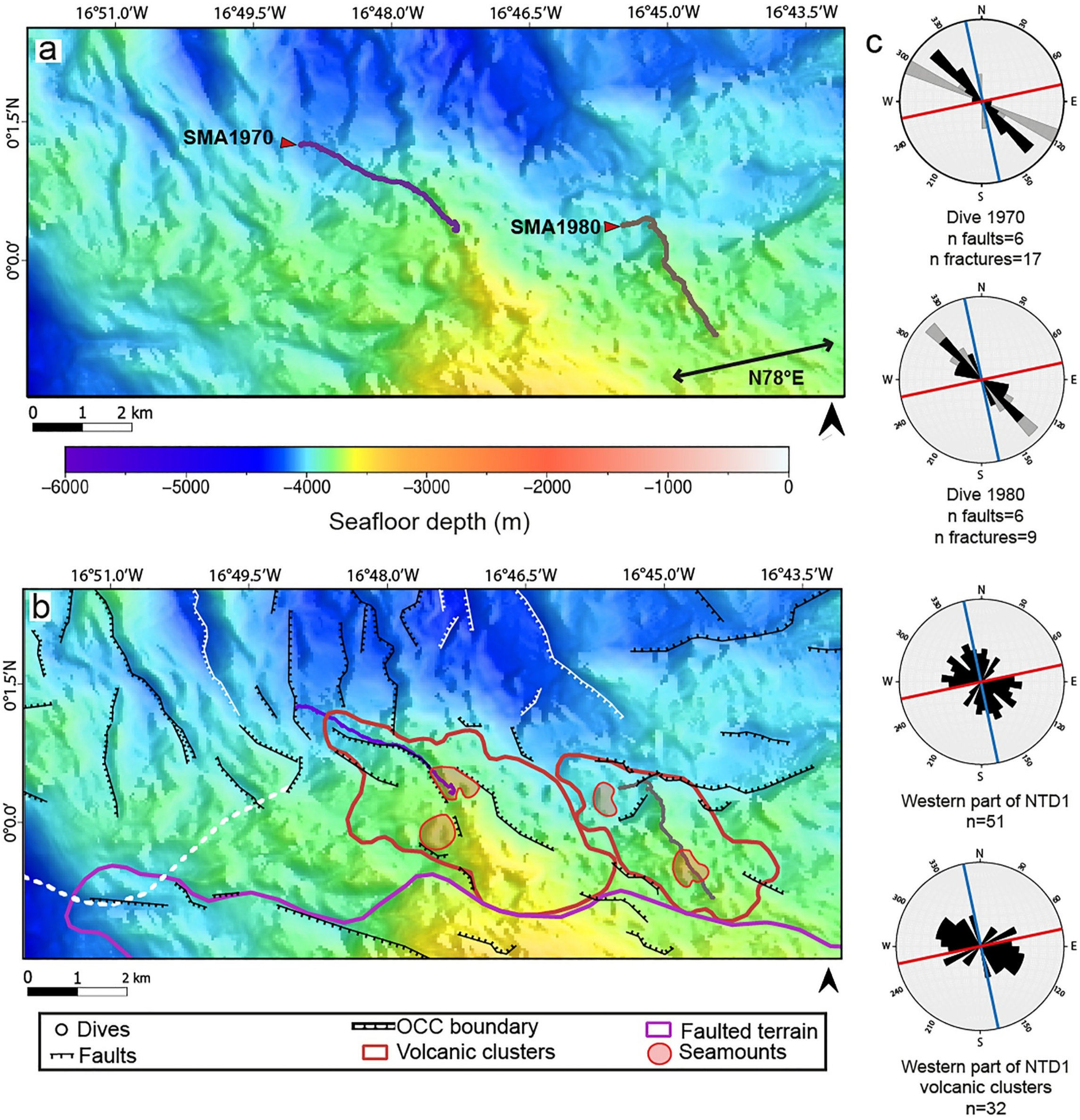

Figure 9. Multibeam bathymetry (a) and (b) and rose diagrams (c) of the western part of NTD1. (b) The red line represents the boundary of volcanic clusters and the purple one that of faulted area. The white dashed line represents the boundary of the oceanic core complex. (c) Rose diagrams of fault (black) and fracture (light gray) orientations along the two dives (top) and at regional scale (bottom), n is the number of faults or fractures. Red and blue lines as in Figure 8. (d) Backscatter mosaic with high intensity shown in light tones (e) structural map of the western part of NTD1.

4.5. Non-Transform Discontinuity 2

The NTD2 has a general N110°E trend. The deep, oblique basin in its center is bounded to the east by volcanic ridges trending N150–160°E showing terraces, and to the west by N120°E and N150–160°E structures (Figures 6 and 11). The area is affected by a small number of faults, mainly oriented N150–170°E, heavily covered by sediments (Figures 11c–11e). The exploration of the basin during the dive SMA1978 (Figure S14 in Supporting Information S1) shows that the outcrops of pillows are small and sparse, separated by large sedimented areas. Pillow lava flows were observed, with rare sheet flows and a layer of compacted sediments exposed in a fault scarp. Fractures have mainly N160–170°E directions, although some fractures and the two described faults have N120–135°E orientations (Figure 11e).

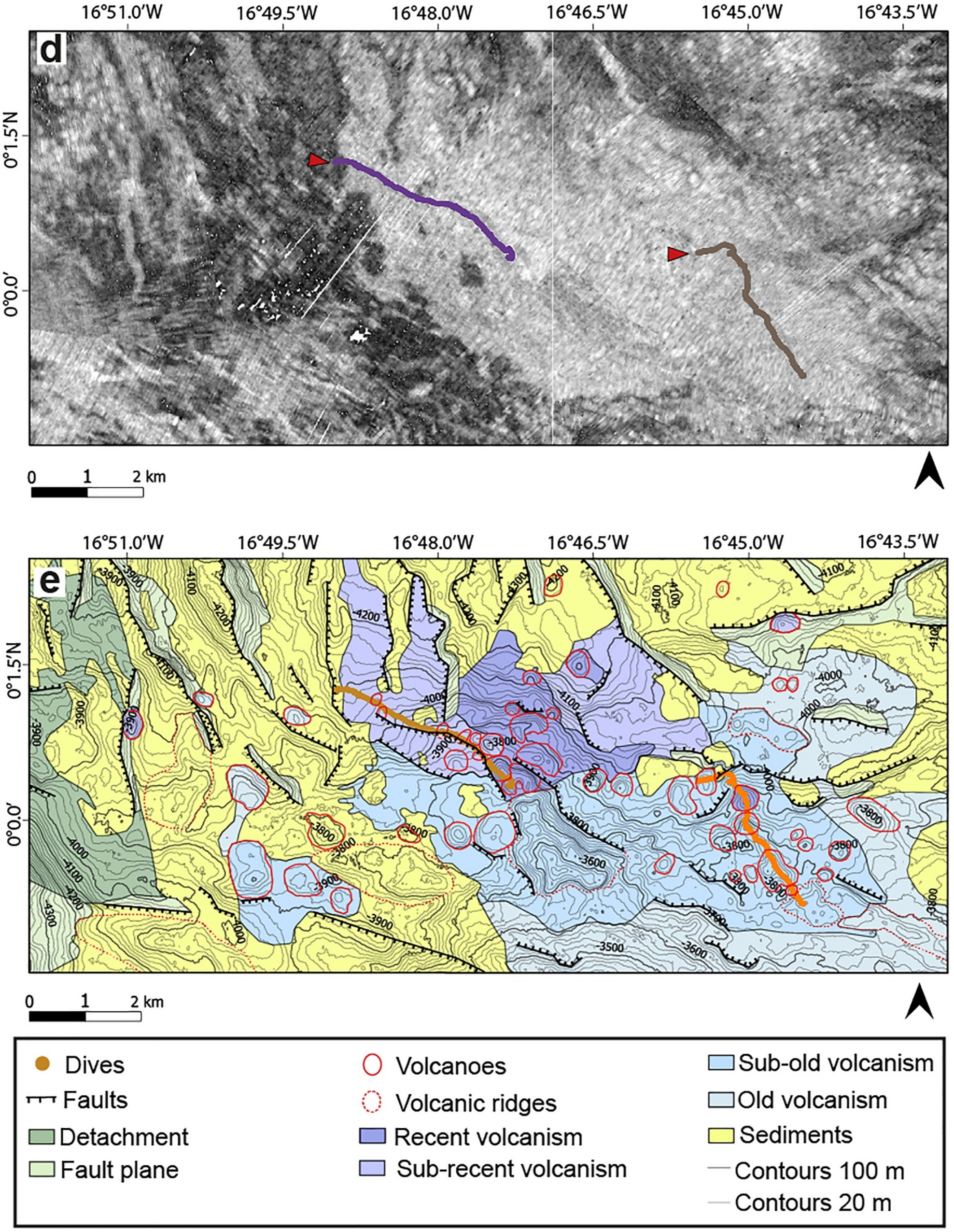

Figure 9. (Continued)

4.6. Quantitative Analysis of Volcanic Morphology

Shape parameters were measured for 129 volcanoes (Figures 12 and 13; Supporting Information S1). The diameter of the base varies between 161 and 1199 m, the height between 21 and 132 m. The height-to-basal diameter ratio varies between 0.04 (flat volcano) and 0.34 (conical). The flatness of volcanoes is between 0.18 (conical) and 0.79 (flat-topped).

Seamounts (namely volcanoes with a diameter >500 m and a height >50 m) show more morphological variability. The flatness values are consistent with those measured for the cones, with seamounts more conical in NTD1 (Figure 13). Seamounts are taller and more voluminous for the ridge segments than for discontinuities and

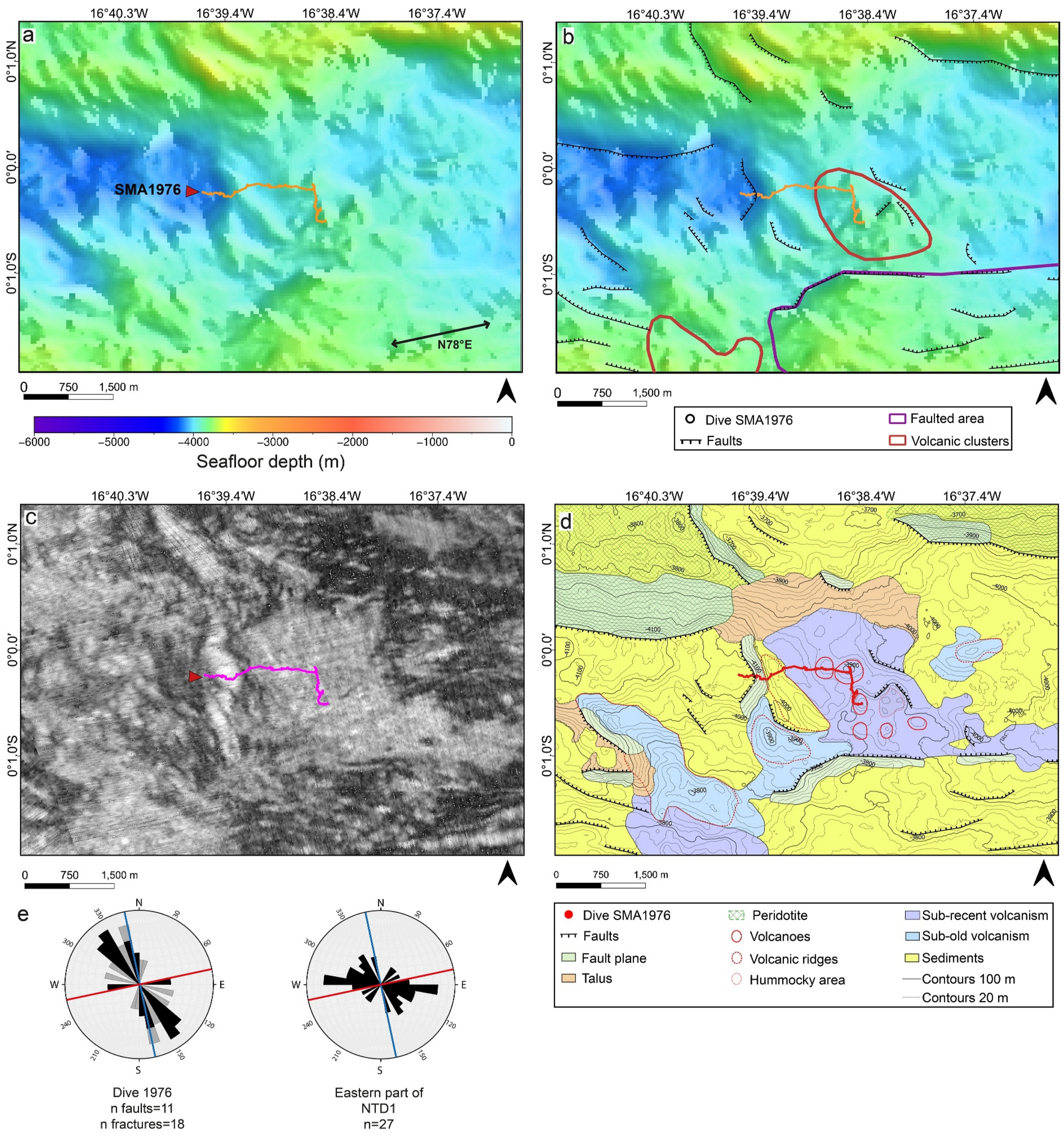

Figure 10. Multibeam bathymetry (a) and (b), backscatter (c) and structural (d) maps of the eastern part of NTD1. The red line in b represents the boundary of volcanic clusters. (e) Rose diagrams of fault (black) and fracture (light gray) orientations along the dive (left) and at regional scale (right), n is the number of faults or fractures. Red and blue lines as in Figure 8.

those of RC2 tend to be the tallest (Figure 13). The density of seamounts is the highest in RC2 and is slightly higher in NTD1 than in RC3 (Table 1).

4.7. ^{40}Ar/^{39}Ar Dating of Recent Volcanic Activity

The step-heating experiments (Figures S15 and S16 in Supporting Information S1) conducted on the four samples allow the calculation of plateau ages with 78.7%–100.0% of total gas released (Table 2 and in Supporting Information S3). This is evidence that the K-Ar clock of these samples was not disturbed and that the calculated ages are reliable. There is also no evidence for ^{40}Ar* excess or mass fractionation, as the ^{40}Ar/^{36}Ar intercept values

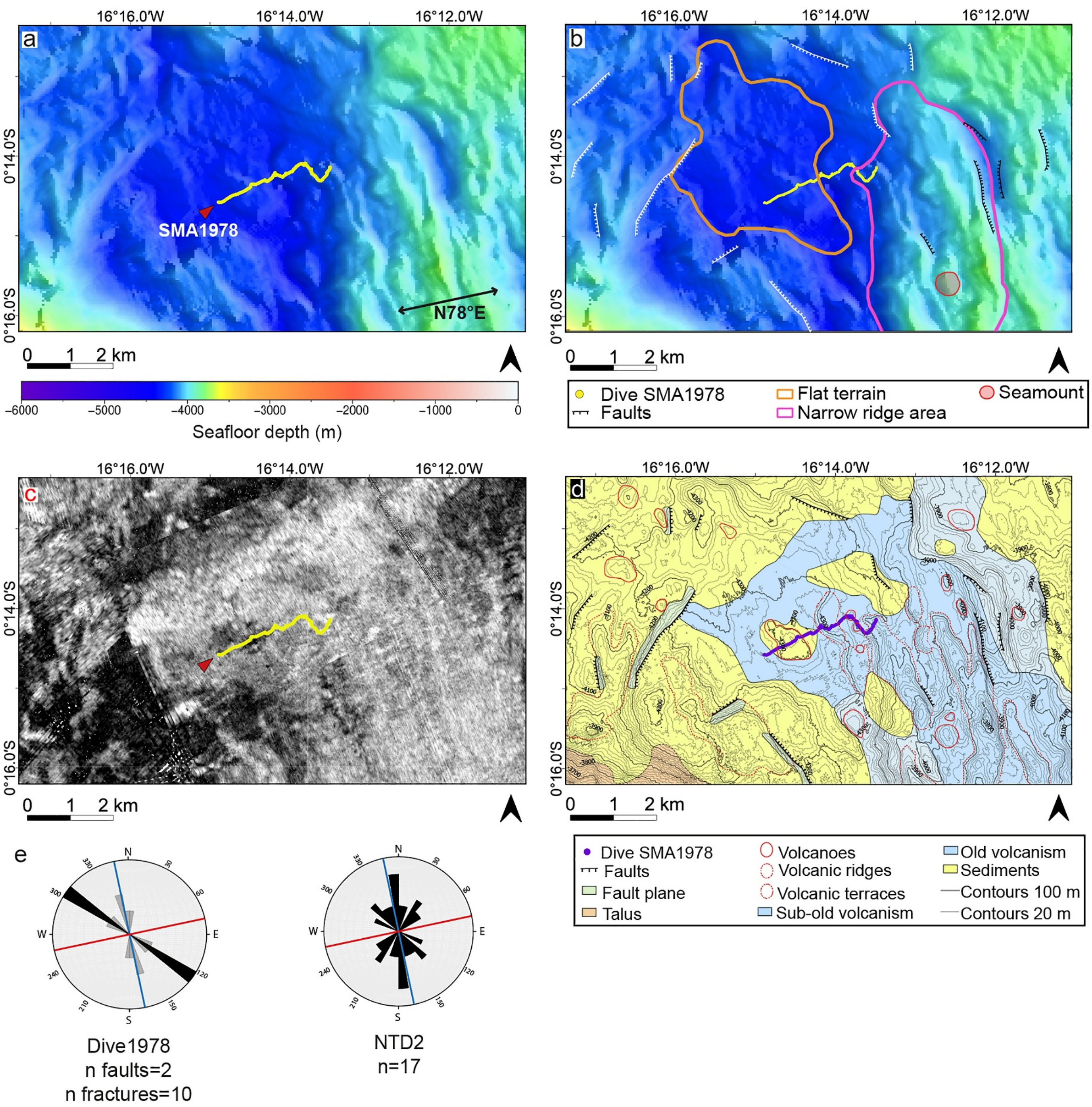

Figure 11. Multibeam bathymetry (a) and (b), backscatter (c) and structural (d) maps of the eastern part of NTD2. The pink line in b represents the boundary of an area composed of narrow volcanic ridges. In b the faults are represented by black and white lines to facilitate reading in dark areas of the map. (e) Rose diagrams of fault (black) and fracture (light gray) orientations along the dive (left) and at regional scale (right), n is the number of faults or fractures. Red and blue lines as in Figure 8.

calculated for the four inverse isochrons (Table 2 and Supporting Information S1, Figures S15 and S16) are, within uncertainties, close to the current atmospheric value.

According to the loss-on-ignition values and the alteration index (A.I.) values (Supporting Information S3), we consider that the samples are mostly unaltered. In samples SMA1970-192, SMA1970-200, and SMA1974-279, the A.I. values of the steps defining the plateaus vary from two to almost three times the threshold value. The A.I. values calculated for SMA1975-303 are four times the cutoff. These values are certainly higher than the limit value, but of an order of magnitude compatible with that of slight to moderate alteration. Therefore, we consider that the ^{40}Ar/^{39}Ar dates calculated from the step-heating experiments (Table 2) are reliable and geologically significant, corresponding to the eruption ages.

The ^{40}Ar/^{39}Ar plateau ages of the four samples (Figures S14 and S15 in Supporting Information S1) show that the volcanic activity is recent. In the western part of NTD1 (dive SMA1970) the two ages obtained for SMA1970-192

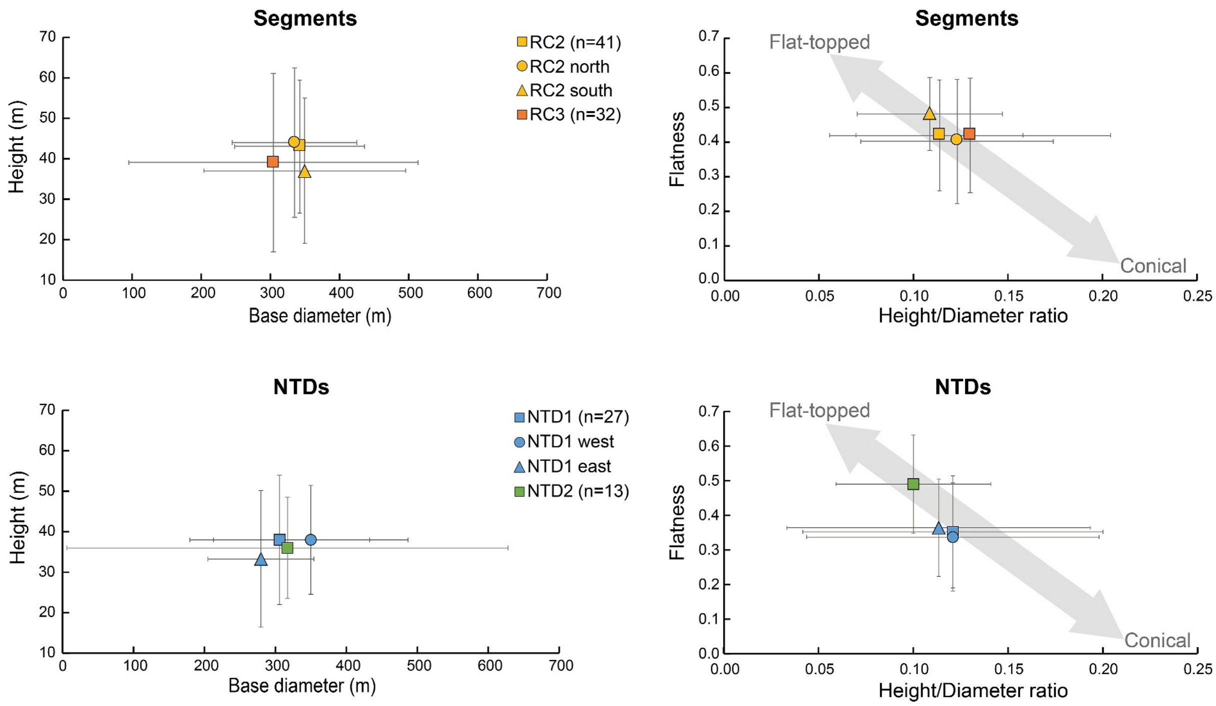

Figure 12. Median morphology parameters of cones for each segment and discontinuity. The bars are interquartile range. n is the number of counted cones.

and SMA1970-200 are 83.1 ± 19.8 ka and 56.1 ± 27.4 ka, respectively. The sample SMA1970-192 was collected in a highly sedimented fracture, located in a flat area. Its radiometric age, younger than 100 ka, is slightly younger than the age expected for a thick sediment cover. The sample SMA1970-200 was collected on a fault wall, where sedimentation can be easily disturbed giving unreliable sediment-estimated ages.

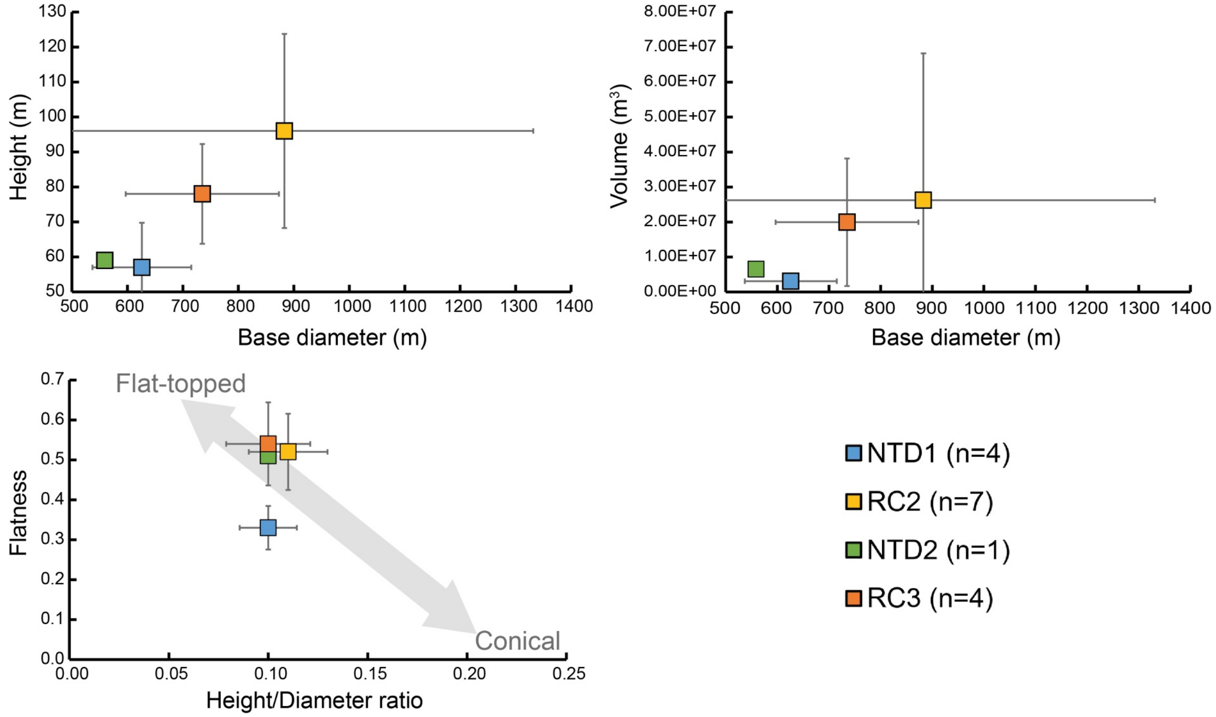

Figure 13. Median morphology parameters of seamounts for each segment and discontinuity. The bars are interquartile range. n is the number of counted seamounts.

The sample SMA1976-318 collected in the eastern part of the NTD1 (dive SMA1976), dated at 64.0 ± 17.6 ka, appears to be contemporaneous with samples collected in the western part of NTD1. The sample was collected on a volcano moderately covered by sediments which corresponds to an age between ∼40 and 100 ka. The radiogenic age and the relative ages established based on the sediment cover are coherent.

The sample SMA1974-279, collected in the eastern part of the segment RC2 (dive SMA1974) with an age of 136.5 ± 11.1 ka, is older than those collected in NTD1. Its radiogenic age is also coherent with the relative age, since it was sampled in a heavily sedimented part of the valley (estimated to ∼100–150 ka).

Table 1
Summary of the Seamount Characteristics in the Neo-Volcanic Zones of NTD1, RC2, and RC3

	NTD1	RC2	RC3
NVZ surface (km^2)	119	161	152
Number of seamounts	4	7	4
Number of seamounts/100 km^2	3.4	4.3	2.6

5. Discussion

5.1. Expression of Tectonic Extension With Distance From the Romanche Transform Fault

Along the ridge segments, oblique normal faults are observed up to more than 50 km from the ERRTI. The obliquity, that is, the angle between the fault direction and the normal to the spreading direction, varies between ∼0° and 50° in segment RC2 and between ∼0° and 30° in RC3 segment (Figure 14). The fault orientation systematically changes along the ridge axis with the distance to the Romanche TF going from oblique in NTD1 close to the TF, to normal to the spreading direction in RC3 far from the TF (Figure 14). The rotation of the fault system attests for a rotation of the horizontal stress field that becomes progressively more extensional away from the TF. We interpret these variations to be controlled by the extreme transform cold edge effect.

A rotation of the stress field with an increasing component of shear stress approaching the TF was first suggested by Fox and Gallo (1984). In their model, slow-spreading RTIs are characterized by the presence of oblique faults due to the shear stress induced by the welding between the axial upper mantle and the lithosphere across the TF. This type of oblique faults has been described in RTIs along the MAR (Karson & Dick, 1983; Lawson et al., 1996; Mamaloukas-Frangoulis et al., 1991; Otter et al., 1984). Fox and Gallo (1984) show that the extent of this shear stress effect increases with the size of the mantle weld, which in turn depends on the thickness of the truncating lithosphere, or the age offset. In case of slow-spreading ridges affected by large TF, oblique structures develop over 20–30 km from the RTI (Fox & Gallo, 1984). The fault obliquity in our study area extends up to ∼50 km

Table 2
Summary of ^{40}Ar/^{39}Ar Data From Incremental Heating Experiments on Groundmass Splits

Samples Lab file #.		SMA1970-192 FG-3064 to FG-3075	SMA1970-200 FG-3074 to FG-3083	SMA1974-279 FG-3044 to FG-3053	SMA1976-318 FG-3054 to FG-3063
wt. (mg)		135	142	148	143
K/Ca (total)		0.085	0.054	0.250	0.193
Total FusionAge (ka)		93.3 ± 26.8	76.6 ± 32.0	117 ± 13.1	53.7 ± 23.9
Age spectrum	Increments used (°C)	600–1171	602–1167	605–1023	668–1168
	^{39}Ar (%)	100.0	100.0	78.7	98.4
	Age ± 1 σ[a] (ka)	**83.1 ± 19.8**	**56.1 ± 27.4**	**135.3 ± 11.1**	**63.0 ± 17.4**
	MSWD	0.10	0.23	0.31	0.01
Isochron analysis	n/N	10 of 10	10 of 10	8 of 10	9 of 10
	MSWD	0.16	0.04	0.46	0.02
	^{40}Ar/^{36}Ar ± 1σ intercept	299.0 ± 0.7	300.5 ± 1.2	297.7 ± 0.9	298.1 ± 0.8
	Age ± 1 σ[a] (ka)	69.6 ± 25.3	–	149.9 ± 18.3	74.6 ± 25.2
	F Spreading Factor	1.1%	–	3.7%	1.4%

Note. Ages calculated relative to Acs-2 standard at 1.1891 Ma (Niespolo et al., 2017) and the total ^{40}K decay constant of Renne et al. (2011). Plateau ages, isochron regressions, probability of fit estimates as well as all errors were calculated using ArArCalc (Koppers, 2002) and following the criteria defined in Schaen et al. (2021). The bold values are the plateau ages. [a]Full external error, included sources of systematic error: ^{40}K(ec,p)^{40}Ar and ^{40}K(β-, n) ^{40}Ca decay constants, the ^{40} K/K abundance ratio, the measurement of the primary K–Ar standard and the subsequent calibrations of the secondary ^{40}Ar/^{39}Ar standards (Koppers, 2002). F: Spreading factor of Jourdan et al. (2009).

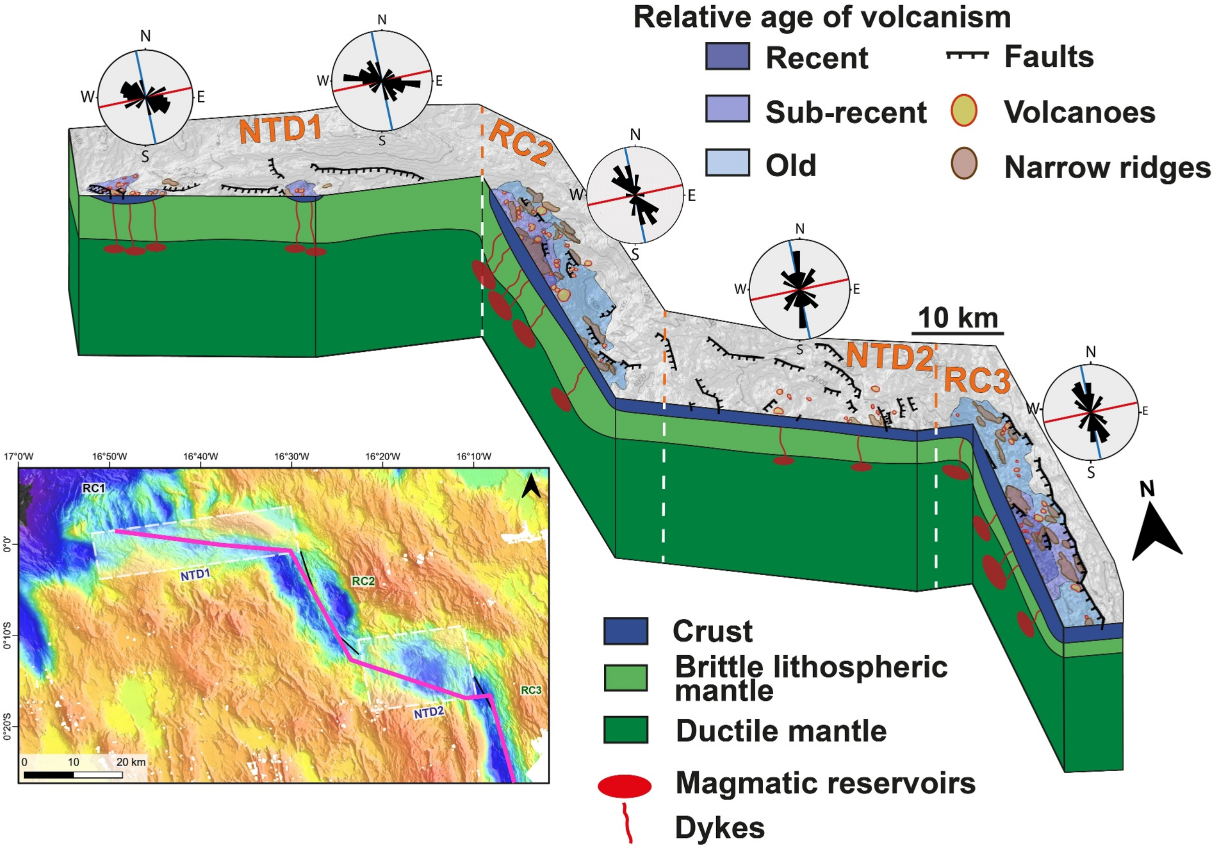

Figure 14. 3D sketch illustrating the observed structure of the MAR axis, including volcanic and tectonic structures and the possible mantle structure deduced from the surface observations. The fault obliquity in NTD1 varies between 30 and 90°, while the faults in RC2 and RC3 have an obliquity between 0 and 50°. In NTD1, the volcanic activity is present as clusters, the basaltic crust is sparse and thin. The oblique segment RC2 seems to be more supplied by magma than the segment RC3, since RC2 is symmetric and includes the largest seamounts of the area. The faults and segments orientation as well as the magmatic activity suggest that the lithosphere is thick beneath NTD1 and becomes progressively thinner southwards. The thicknesses of the crust and lithosphere are indicative, as the vertical scale is unconstrained by geophysical data. Bottom left: bathymetric map of the MAR axis at the ERRTI, the pink line corresponds to the section trace.

from the ERRTI (i.e., the southern end of RC2), an extent consistent with the very large offset of the Romanche TF and the likely large thickness of the weld region.

The 35 km-long NTD1 is one of the longest of the MAR. Despite a trend nearly subparallel to the Romanche TF, this discontinuity does not display a narrow shear zone. Instead, the observed normal faults have a 30–90° obliquity (Figures 9c and 10e). These fault orientations are characteristic of discontinuities where the shear stress component dominates with respect to the extensional stress, with a component of strike-slip motion along the faults (Fox & Gallo, 1984; Grindlay & Fox, 1993). It has been shown that the width of the NTDs increases with the lithosphere thickness (Gomez et al., 2006; Mauduit & Dauteuil, 1996). The large width of NTD1 likely reflects the presence of a thick lithosphere under the discontinuity (Figure 14).

The mantle thermal setting inferred from the 3D mantle flow model of the ERRTI by Ligi et al. (2005) predicts that the cold-edge effect extends as far as 80 km from the intersection. The increase of $(Sm/Yb)_N$ ratio toward the TF described by Ligi et al. (2005) suggests a progressive increase of the average melting depth, consistent with an increasing lithospheric thickness toward the TF. An independent test of the lithosphere thickness can be derived by the pressure of crystallization of the erupted basalts. The crystallization starts in the axial magma chambers generally located at the base of the lithosphere (Wanless & Behn, 2017), hence the pressure of crystallization can be used as a proxy of the lithosphere thickness. We calculated the crystallization pressure of basalt using the whole-rock composition of samples pre-selected for the dating with the barometer of Herzberg (2004). We noticed a decrease in the pressure of crystallization from RC2 (0.52 ± 0.21 GPa, ~17.3 km using a mantle density of 3.33 g/cm^3) to RC3 (0.20 ± 0.14 GPa, ~6.8 km) (Supporting Information S1, Figure S17; Supporting

Information S4). A relatively thick lithosphere beneath RC2, that is, at ~50 km from the RTI, could explain the existence of oblique faults and the slight obliquity of the segment.

Oblique normal faults were also observed in dives located close to the extremities of segments RC2 and RC3 (Figures 7c and 8c). These faults are thought to accommodate the shear stress near the discontinuities (Autin et al., 2010; Gomez et al., 2006; Spencer et al., 1997).

5.2. The Magmatic Activity Along the Axial Domain

Previous studies predicted a regional decrease of the melt production toward the TF, including a ~30 km-long band where the basaltic crust would be nearly absent (Bonatti et al., 1996, 2001; Ligi et al., 2005). We observe volcanic clusters in NTD1 (Figures 9 and 10), only 10 km away from the TF, showing that melt is produced in this area, even if in small amounts. Further south, segments RC2 and RC3 have well-defined AVRs with recent lava flows, large seamounts, cones and narrow ridges (Figures 7–10 and 14). In this section, we use the flow morphologies, as well as the size and density of seamounts along the NVZ to discuss the magma supply and the formation of the volcanic constructions.

We observe a general decrease of the volcanic activity along axis toward the ERRTI. From the whole-rock composition of the samples pre-selected for the dating, we estimated the melting conditions (temperature and pressure) using the method of Lee et al. (2009). The progressive decrease of the cold-edge effect with the distance from the Romanche TF could be consistent with the calculated melting temperatures (Supporting Information S1, Figure S17; Supporting Information S4) which on average seem to increase very slightly between RC2 (1,400 ± 48°C) and RC3 (1,421 ± 21°C). A similar and more marked trend is observed for the NTDs with melting temperatures increasing from 1,375 ± 22°C under NTD1 to 1,442 ± 41°C under NTD2.

The landscapes in the study area are heavily dominated by pillow lavas with only rare occurrences of sheet or massive lava flows, an observation which suggests that the effusion rates along this section of the MAR are generally low. The rare observed sheet flows likely result from short-term, local variations of eruption parameters (effusion rate, lava viscosity, cooling rate or pre-existing slope). However, dives explored mostly steep slopes to avoid sedimented areas, so that the choice of the dive tracks might have induced an observation bias, leading us to underestimate the abundance of sheet flows.

To gain further insights into variations of volcanic styles, we compared the seamount morphometric parameters to those of segments of other ridges described in previous studies (Figure 15), which include the Gakkel Ridge (Cochran, 2008), segments of the SWIR located between the Atlantis II fracture zone and the Rodrigues triple junction (Mendel & Sauter, 1997) and segments of the MAR located between the Atlantis and Kane TFs (Smith & Cann, 1992; Smith et al., 1995). The range in heights obtained in RC2 and RC3 (62–132 m) is similar to those described in Gakkel Ridge (50–160 m), but smaller than those in the SWIR (60–512 m) and in the MAR (50–650 m, Smith & Cann, 1992) (Figure 15). We do observe a few flat-topped volcanoes in RC2 and RC3. Smith et al. (1995) proposed that volcanoes formed at high eruption rates will preferentially pour out laterally instead of growing up vertically. These edifices have a low height-to-basal diameter ratio, forming flat-topped volcanoes. Eruption rates in RC2 and RC3 segments appear to locally reach values that allow the formation of flat-topped volcanoes.

The density of seamounts in segment RC2 (~4.3 per 100 km^2) is similar to the lowest values observed in some MAR segments (~4.6–4.9 per 100 km^2; Smith & Cann, 1992) and in the Western Volcanic Zone of Gakkel Ridge (~5.2 per 100 km^2; Cochran, 2008). The estimated density in the segment RC3 (~2.6 per 100 km^2) is comparable to the lowest density calculated in the Western Volcanic Zone of Gakkel Ridge (~2.4 per 100 km^2). The size and the density of seamounts described in segments RC2 and RC3 are comparable to those observed in Gakkel Ridge and smaller than those of the MAR and SWIR segments. We interpret this to result from a low magmatic supply compared to the slow spreading rate (Cochran, 2008; Mendel & Sauter, 1997), linked to the cold edge effect (i.e., low magma productivity and high lithospheric thickness) in our study area.

The pattern of volcanism within non-transform discontinuities confirms the low eruption rates in the area and the general decrease of magma input closer to the ERRTI. In NTD2, the edifices mostly form narrow volcanic ridges and volcanoes are rare, while in NTD1 volcanoes form clusters (Figures 9–11). The size and morphology of the volcanoes in both discontinuities (Figures 12 and 13) indicate that eruption rates are generally low. In NTD1 the edifices are likely built with lower eruption rates than those of NTD2.

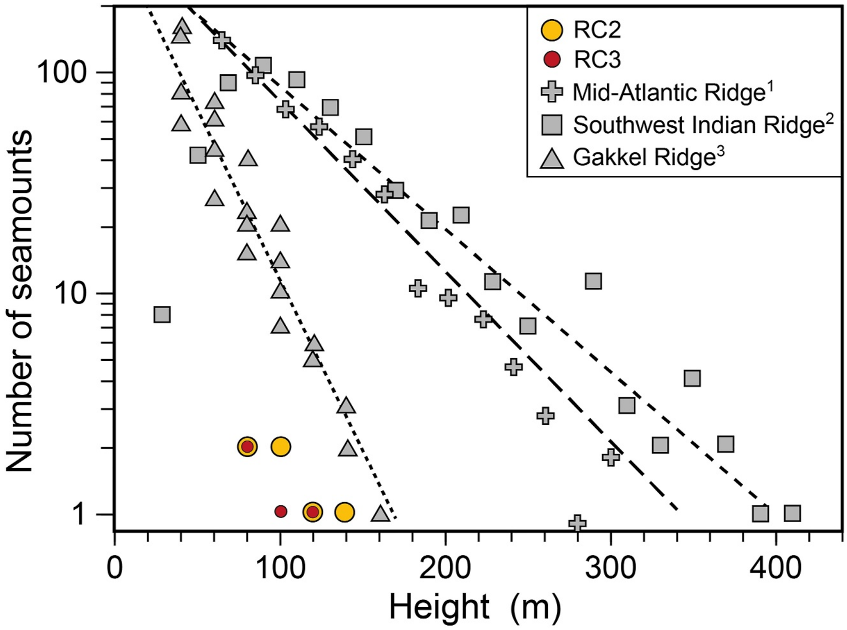

Figure 15. Cumulative number of seamounts as a function of their height, in 20 m-wide bins, in RC2 and RC3 segments compared to previous studies. [1]Smith and Cann, 1992; [2]Mendel and Sauter, 1997; [3]Cochran, 2008.

We interpret the volcanic morphologies within segment RC2 to reflect a spatial and temporal change in magma supply. The northern part of the AVR is wider and higher above the valley floor than the southern part (Figure 7). We identified five seamounts in the northern part of the axial valley, against two in the southern part. In addition, the northwestern portion of RC2 appears to be young, with recent pillow lava flows and a thin sediment cover, while the eastern and southern parts, covered by more sediments at the outcrop and segment scales, seem to be older (Figure 7). These observations suggest either that the magma recently migrated and was extracted in the northern part, or that the supply of magma is more vigorous in the northern part than in the southern part.

Contrary to previous observations (Bonatti et al., 1996, 2001; Ligi et al., 2005), we documented the presence of volcanic activity throughout the study area, including in NTD1 as close as 10 km south to the intersection. In addition, despite its proximity to the TF, RC2 appears to be more magmatic than expected from numerical models. Those models from Ligi et al. (2005), based on Bonatti et al. (1996, 2001) observations, modeled mantle temperature and magmatic production in a steady-state temperature regime and uniform mantle composition. The volcanic activity in NTD1 and the magma production in the northern part of RC2 could be related to a variation in mantle composition. Previous geochemical studies of RC2 highlighted the presence of mantle lumps enriched in trace elements and volatiles that would melt more easily (Le Voyer et al., 2015; Schilling et al., 1994; Verhoest, 2022). We propose that such a mantle heterogeneity might be responsible for a larger magma supply in the northern part of RC2 and under NTD1, where the mantle temperatures are the lowest in the area (Supporting Information S1, Figure S17).

5.3. Relationships Between Tectonics and Volcanism With Distance From the Romanche Transform Fault

To understand the processes generating the oceanic crust near the ERRTI we evaluated how volcanic and tectonic events interact as a function of the distance from the Romanche TF. Non-transform discontinuities are key geological objects in this context, accommodating the strike-slip stresses due to axial offsets. Along our study area, the structures of NTD1 and NDT2 show contrasting stories. NTD2, located ~60 km south of the intersection, displays a central basin approximately 40–50° oblique to the ridge axis direction and is affected by faults normal to the spreading direction. This is a structure similar to other NTDs observed along the MAR (Grindlay et al., 1991; Grindlay & Fox, 1993). In this type of discontinuity (i.e., oblique shear zone discontinuities) volcanism is limited and tends to form narrow or hummocky ridges (Briais et al., 2000; Gràcia et al., 1997; Spencer et al., 1997). NTD1, which is closer to the TF, is a transtensive discontinuity, where sparse narrow ridges and characteristic clusters of individual volcanoes are observed (Figure 16). In oblique mid-ocean ridge sections

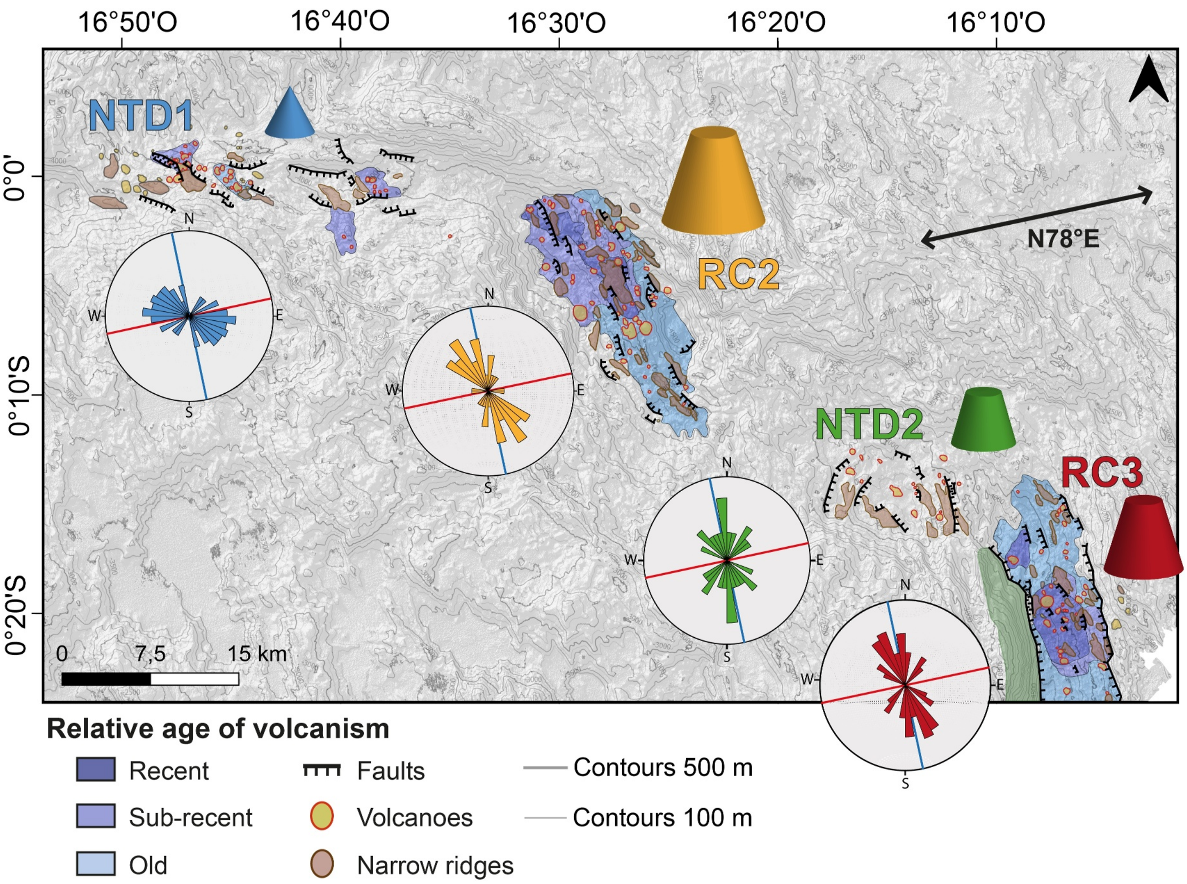

Figure 16. Schematic structural map of the MAR axis, from NTD1 to the northern part of RC3. Rose diagrams of fault orientations for each segment and discontinuity. The schematic cones represent the relative size and morphology of seamounts.

poorly supplied by magma, faults tend to be short and form an en-echelon pattern (Gomez et al., 2006). En-echelon structures can restrict the size of magma reservoirs, leading to the construction of individual seamounts rather than ridges (Behn et al., 2004). We interpret the volcanic clusters of NTD1 to result from fissure eruptions of small quantities of magma. Similar volcanic centers with cones have been described in inter-segments of the Southwest Indian Ridge (Cannat et al., 2008). They are associated with faults oblique and normal to the spreading. The difference in volcano-tectonic structure of NTD1 and NTD2 supports the hypothesis of a thicker lithosphere in the north.

Due to the cold edge effect, we could expect RC2 to be less supplied in magma than RC3. However, the height and density of seamounts are higher in RC2 than in RC3 (Figure 13), which could be due to a thicker lithosphere beneath RC2 and/or a temporary lower magma supply in RC3. According to Smith and Cann (1992), the height of seamounts is related to the depth of the source which depends on the thickness of the brittle-ductile transition (delimited by the isotherm 750°C). The height of seamounts will also depend on the total magma supply and the duration of the eruption (Wilson et al., 1992). Hence, a thicker lithosphere under RC2 combine with a current lower magma supply under RC3 that RC2, can explain the difference in size of the seamounts between the two segments (Mendel & Sauter, 1997; Smith & Cann, 1992; Wilson et al., 1992). The variations of the basalt crystallization pressure, used as a proxy of the lithosphere thickness, with higher estimated pressures on average under RC2 than under RC3, are consistent with the presence of a thicker lithosphere beneath RC2 (Supporting Information S1, Figure S17). Part of the apparent contrast between segments RC2 and RC3 could thus result from variations in the lithosphere thickness.

Another possible explanation for the lower density and size of seamounts currently observed in the segment RC3 compared to RC2 is a temporary lower magma supply in RC3. This hypothesis is supported by the observation of a detachment fault in the northern part of RC3, which suggests that the magma input in this part of RC3 has recently been lower (Behn & Ito, 2008; Buck et al., 2005; Escartín et al., 2008; Olive & Dublanchet, 2020).

Defining which segment is magmatically more robust would require estimating the crustal thickness of each segment using high-resolution seismic reflection and refraction profiles. It would also require a morphological study of the entire segment RC3, which is currently not possible due to the lack of high-resolution bathymetry.

In the northwestern part of segment RC2, faults and volcanic alignments are orthogonal to the spreading direction (~N150–160°E), while in the oldest terrains, they are oblique (~N130–140°E) (Figure 7). This variation in faults orientation is not related to minor changes in spreading direction, first because they would affect the entire axis, including RC3, which is not observed, and second because such changes in plate motion have not been described for recent times (DeMets & Merkouriev, 2019). It is likely due to the local magma supply. According to Cannat et al. (2008), a higher melt supply leads to the reorientation of a ridge segment by modifying the rheology of the axial lithosphere. In the northwestern part of RC2, the volcanoes are younger, more numerous and voluminous than in the eastern and southern parts (Figure 7). Therefore, we interpret the orientations of the faults and volcanic systems as reflecting a recent higher supply magma in the northwestern part of the segment, leading to a change in the orientation of the stress field and the formation of faults normal to spreading.

The distribution of fault directions in NTD1, especially in the eastern part of NTD1, may also be related to a recent, local pulse of magmatism. The presence of peridotite and the distribution of volcanic terrains as clusters of volcanoes in NTD1 suggest a thin and discontinuous basaltic crust (Bonatti et al., 1996), a setting explaining the oblique direction of most normal faults, with a component of shear (Figure 14). But in this area dominated by shear stress, the volcanic clusters are associated with faults orthogonal to spreading (N150–160°E) (Figures 9 and 10). This suggests that the presence of magma, even in limited volume, may be sufficient to affect the rheology of the lithosphere and fault orientation.

6. Conclusion

From submarine dive videos, bathymetric and reflectivity data, we described the NVZ of the MAR from the eastern intersection between the Romanche TF to ~120 km south of it. Our new geological maps present the volcanic and tectonic structures, together with the relative ages of lava flows based on sediment thickness. These first-order observations were completed by the quantification of volcano morphology and by geochronological data.

Our new interpretation of the NVZ structure shows that the studied axial domain is composed of three ridge segments (RC1–RC3) offset by two non-transform discontinuities (NTD1-NTD2). The new high-resolution observations reveal that small amounts of magma are produced close to the ERRTI (~10 km south) in NTD1.

We documented a general increase of volcanic activity along axis with the distance from the ERRTI. We also noted a progressive change in the fault directions with the distance from the Romanche TF, from highly oblique in NTD1, to normal to spreading in the segment RC3. The segment RC2 appears slightly oblique to the spreading direction. These progressive variations could be linked to the decrease of the cold edge effect marked by a decrease of the lithosphere thickness and of the shear stress with increasing distance from the TF.

The seamount population and lava morphologies in RC2 and RC3 suggest that both segments are magmatically less robust than regular magmatic MAR segments. The melt production seems to increase abruptly along the axis in the northern part of RC2, since this segment appears to be more supplied by magma than predicted by previous numerical thermal models. The larger melt supply could result from melting of a more fusible lump of mantle under the northern part of RC2 and NTD1. However, the presence of higher edifices and density of seamounts in RC2 compared to RC3 could be partly due to a recent decrease of melt production in the north of RC3, to the thick lithosphere beneath RC2, or both.

In NTD1 and RC2, which are strongly affected by the shear stresses induced by the Romanche TF, the faults and volcanic alignments are mostly oblique to the spreading direction. In areas where the recent magma supply is higher such as the volcanic clusters of NTD1 and in the northwestern parts of the segment RC2, we observe faults and fractures less oblique to spreading. The local increase of magma supply modifies the rheology of the axial lithosphere, influencing the stress field and allowing for the reorientation of faults.

Data Availability Statement

Bathymetry grids and backscatter mosaics along the axis of the Mid-Atlantic Ridge south of the Romanche transform fault used for this work are available via SEANOE archive website at Grenet, Maia, Hamelin, Briais, and Brunelli (2023). Videos from the Nautile fixed and mobile cameras on the neo volcanic zone described in this study are available in SEANOE website at Maia et al. (2023). ^{40}Ar/^{39}Ar ages and major elements composition of basalts analyzed in this study are available in SEANOE website at Grenet, Maia, Hamelin, Briais, Guillou, et al. (2023).

Acknowledgments

The ship time for the SMARTIES cruise (Maia et al., 2019; https://doi.org/10.17600/18001107) was granted by the TGIR French Oceanographic Fleet. Bathymetry, backscatter and video images processing and analyzes and ^{40}Ar/^{39}Ar dating received CNRS-INSU financial support through TelluS program, "Campagnes à la mer". L.G. was supported by Région Bretagne (France). Publication fees funded by Université de Bretagne Occidentale through the COUPERIN Consortium. We are grateful to Captain P. Moimeaux and his crew from R/V *Pourquoi Pas?*, to X. Placaud and the Nautile team and to the SMARTIES science party for their help on acquiring and processing the data presented here. We thank J-P. Oldra and P. Nonnotte for their help in sample preparation and C. Liorzou for major element analysis. We also thank Neil Mitchell, Darin Schwartz and two anonymous reviewers for their constructive reviews that led to significant improvements in the manuscript.

References

Abercrombie, R. E., & Ekström, G. (2001). Earthquake slip on oceanic transform faults. *Nature*, *410*(6824), 74–77. https://doi.org/10.1038/35065064

Agius, M. R., Harmon, N., Rychert, C. A., Tharimena, S., & Kendall, J.-M. (2018). Sediment characterization at the equatorial mid-Atlantic Ridge from *P* -to- *S* teleseismic phase conversions recorded on the PI-LAB experiment. *Geophysical Research Letters*, *45*(22), 12244–12252. https://doi.org/10.1029/2018GL080565

Alt, J. C., Honnorez, J., Laverne, C., & Emmermann, R. (1986). Hydrothermal alteration of a 1 km section through the upper oceanic crust, Deep Sea Drilling Project Hole 504B: Mineralogy, chemistry and evolution of seawater-basalt interactions. *Journal of Geophysical Research*, *91*(B10), 10309–10335. https://doi.org/10.1029/JB091iB10p10309

Anderson, R. N., McKenzie, D., & Sclater, J. G. (1973). Gravity, bathymetry and convection in the earth. *Earth and Planetary Science Letters*, *18*(3), 391–407. https://doi.org/10.1016/0012-821X(73)90095-2

Autin, J., Bellahsen, N., Husson, L., Beslier, M.-O., Leroy, S., & d'Acremont, E. (2010). Analog models of oblique rifting in a cold lithosphere: Analog models of oblique rifting. *Tectonics*, *29*(6). https://doi.org/10.1029/2010TC002671

Baksi, A. K. (2007). A quantitative tool for detecting alteration in undisturbed rocks and minerals—I: Water, chemical weathering, and atmospheric argon. *Special Paper 430: Plates, Plumes and Planetary Processes*, *430*, 285–303. https://doi.org/10.1130/2007.2430(15)

Basile, C., Girault, I., Paquette, J.-L., Agranier, A., Loncke, L., Heuret, A., & Poetisi, E. (2020). The Jurassic magmatism of the Demerara Plateau (offshore French Guiana) as a remnant of the Sierra Leone hotspot during the Atlantic rifting. *Scientific Reports*, *10*(1), 7486. https://doi.org/10.1038/s41598-020-64333-5

Behn, M. D., & Ito, G. (2008). Magmatic and tectonic extension at mid-ocean ridges: 1. Controls on fault characteristics. *Geochemistry, Geophysics, Geosystems*, *9*(8). https://doi.org/10.1029/2008GC001965

Behn, M. D., Sinton, J. M., & Detrick, R. S. (2004). Effect of the Galápagos hotspot on seafloor volcanism along the Galápagos spreading center (90.9–97.6°W). *Earth and Planetary Science Letters*, *217*(3–4), 331–347. https://doi.org/10.1016/S0012-821X(03)00611-3

Bonatti, E., Brunelli, D., Fabretti, P., Ligi, M., Asunta Portaro, R., & Seyler, M. (2001). Steady-state creation of crust-free lithosphere at cold spots in mid-ocean ridges. *Geology*, *29*(11), 979. https://doi.org/10.1130/0091-7613(2001)029<0979:SSCOCF>2.0.CO;2

Bonatti, E., Ligi, M., Carrara, G., Gasperini, L., Turko, N., Perfiliev, S., et al. (1996). Diffuse impact of the Mid-Atlantic Ridge with the Romanche transform: An ultracold ridge-transform intersection. *Journal of Geophysical Research*, *101*(B4), 8043–8054. https://doi.org/10.1029/95JB02249

Bonatti, E., Seyler, M., & Sushevskaya, N. (1993). A cold suboceanic mantle belt at the Earth's equator. *Science*, *261*(5119), 315–320. https://doi.org/10.1126/science.261.5119.315

Briais, A., Sloan, H., Parson, L. M., & Murton, B. J. (2000). Accretionary processes in the axial valley of the Mid-Atlantic Ridge 27° N–30° N from TOBI side-scan sonar images. *Marine Geophysical Researches*, *21*(1/2), 87–119. https://doi.org/10.1023/A:1004722213652

Buck, W. R., Lavier, L. L., & Poliakov, A. N. B. (2005). Modes of faulting at mid-ocean ridges. *Nature*, *434*(7034), 719–723. https://doi.org/10.1038/nature03358

Canales, J. P., Detrick, R. S., Lin, J., Collins, J. A., & Toomey, D. R. (2000). Crustal and upper mantle seismic structure beneath the rift mountains and across a nontransform offset at the Mid-Atlantic Ridge (35°N). *Journal of Geophysical Research*, *105*(B2), 2699–2719. https://doi.org/10.1029/1999JB900379

Cann, J. R., Blackman, D. K., Smith, D. K., McAllister, E., Janssen, B., Mello, S., et al. (1997). Corrugated slip surfaces formed at ridges-transform intersections on the Mid-Atlantic Ridge. *Nature*, *385*(6614), 329–332. https://doi.org/10.1038/385329a0

Cann, J. R., & Smith, D. K. (2005). Evolution of volcanism and faulting in a segment of the Mid-Atlantic Ridge at 25°N. *Geochemistry, Geophysics, Geosystems*, *6*(9). https://doi.org/10.1029/2005GC000954

Cannat, M., Sauter, D., Bezos, A., Meyzen, C., Humler, E., & Le Rigoleur, M. (2008). Spreading rate, spreading obliquity, and melt supply at the ultraslow spreading southwest Indian ridge: Southwest Indian ridge spreading rate. *Geochemistry, Geophysics, Geosystems*, *9*(4). https://doi.org/10.1029/2007GC001676

Cochran, J. R. (2008). Seamount volcanism along the Gakkel Ridge, Arctic ocean. *Geophysical Journal International*, *174*(3), 1153–1173. https://doi.org/10.1111/j.1365-246X.2008.03860.x

Colman, A., Sinton, J. M., White, S. M., McClinton, J. T., Bowles, J. A., Rubin, K. H., et al. (2012). Effects of variable magma supply on mid-ocean ridge eruptions: Constraints from mapped lava flow fields along the Galápagos spreading center: Gsc volcanic eruptions. *Geochemistry, Geophysics, Geosystems*, *13*(8). https://doi.org/10.1029/2012GC004163

Dannowski, A., Grevemeyer, I., Phipps Morgan, J., Ranero, C. R., Maia, M., & Klein, G. (2011). Crustal structure of the propagating TAMMAR ridge segment on the Mid-Atlantic Ridge, 21.5°N. *Geochemistry, Geophysics, Geosystems*, *12*(7), a–n. https://doi.org/10.1029/2011GC003534

DeMets, C., & Merkouriev, S. (2019). High-resolution reconstructions of south America plate motion relative to Africa, Antarctica and north America: 34 Ma to present. *Geophysical Journal International*, *217*(3), 1821–1853. https://doi.org/10.1093/gji/ggz087

Duncan, R. A., & Hogan, L. G. (1994). Radiometric dating of young MORB using the ^{40} Ar- ^{39} Ar incremental heating method. *Geophysical Research Letters*, *21*(18), 1927–1930. https://doi.org/10.1029/94GL01375

Dziewonski, A. M., & Anderson, D. L. (1984). Seismic Tomography of the Earth's Interior: The first three-dimensional models of the earth's structure promise to answer some basic questions of geodynamics and signify a revolution in earth science. *American Scientist*, *72*(5), 483–494.

Escartín, J., Mével, C., MacLeod, C. J., & McCaig, A. M. (2003). Constraints on deformation conditions and the origin of oceanic detachments: The Mid-Atlantic Ridge core complex at 15°45′N: Mid-Atlantic Ridge oceanic detachment. *Geochemistry, Geophysics, Geosystems*, *4*(8). https://doi.org/10.1029/2002GC000472

Escartín, J., Smith, D. K., Cann, J., Schouten, H., Langmuir, C. H., & Escrig, S. (2008). Central role of detachment faults in accretion of slow-spreading oceanic lithosphere. *Nature*, *455*(7214), 790–794. https://doi.org/10.1038/nature07333

Fink, J. H., & Griffiths, R. W. (1992). A laboratory analog study of the surface morphology of lava flows extruded from point and line sources. *Journal of Volcanology and Geothermal Research*, *54*(1–2), 19–32. https://doi.org/10.1016/0377-0273(92)90112-Q

Fox, C. G., Murphy, K. M., & Embley, R. W. (1988). Automated display and statistical analysis of interpreted deep-sea bottom photographs. *Marine Geology*, *78*(3–4), 199–216. https://doi.org/10.1016/0025-3227(88)90109-0

Fox, P. J., & Gallo, D. G. (1984). A tectonic model for ridge-transform-ridge plate boundaries: Implications for the structure of oceanic lithosphere. *Tectonophysics*, *104*(3–4), 205–242. https://doi.org/10.1016/0040-1951(84)90124-0

GEBCO Compilation Group. (2022). GEBCO 2022 grid. https://doi.org/10.5285/e0f0bb80-ab44-2739-e053-6c86abc0289c

Geissler, W. H., Wintersteller, P., Maia, M., Strack, A., Kammann, J., Eagles, G., et al. (2020). Seafloor evidence for pre-shield volcanism above the Tristan da Cunha mantle plume. *Nature Communications*, *11*(1), 4543. https://doi.org/10.1038/s41467-020-18361-4

Gomez, O., Briais, A., Sauter, D., & Mendel, V. (2006). Tectonics at the axis of the very slow spreading southwest Indian ridge: Insights from TOBI side-scan sonar imagery: Southwest Indian ridge tectonics. *Geochemistry, Geophysics, Geosystems*, *7*(5). https://doi.org/10.1029/2005GC000955

Gràcia, E., Bideau, D., Hekinian, R., Lagabrielle, Y., & Parson, L. M. (1997). Along-axis magmatic oscillations and exposure of ultramafic rocks in a second-order segment of the Mid-Atlantic Ridge (33°43'N to 34°07'N). *Geology*, *25*(12), 1059. https://doi.org/10.1130/0091-7613(1997)025<1059:AAMOAE>2.3.CO;2

Gregg, T. K. P., & Fink, J. H. (1995). Quantification of submarine lava-flow morphology through analog experiments. *Geology*, *23*(1), 73. https://doi.org/10.1130/0091-7613(1995)023<0073:QOSLFM>2.3.CO;2

Gregory, E. P. M., Singh, S. C., Marjanović, M., & Wang, Z. (2021). Serpentinized peridotite versus thick mafic crust at the Romanche oceanic transform fault. *Geology*, *49*(9), 1132–1136. https://doi.org/10.1130/G49097.1

Grenet, L., Maia, M., Hamelin, C., Briais, A., & Brunelli, D. (2023). Bathymetry and backscatter grids along the axis of the Mid-Atlantic Ridge south of the Romanche transform fault (0° 02' 30"N - 0° 20' 56"S) [Dataset]. *SEANOE*. https://doi.org/10.17882/95890

Grenet, L., Maia, M., Hamelin, C., Briais, A., Guillou, H., Scao, V., & Brunelli, D. (2023). ^{40}Ar/^{39}Ar ages and major elements composition of basalts of the Mid-Atlantic Ridge axis [Dataset]. *SEANOE*. https://doi.org/10.17882/95914

Grevemeyer, I., Hayman, N. W., Lange, D., Peirce, C., Papenberg, C., Van Avendonk, H. J. A., et al. (2019). Constraining the maximum depth of brittle deformation at slow- and ultraslow-spreading ridges using microseismicity. *Geology*, *47*(11), 1069–1073. https://doi.org/10.1130/G46577.1

Griffiths, R. W., & Fink, J. H. (1992). Solidification and morphology of submarine lavas: A dependence on extrusion rate. *Journal of Geophysical Research*, *97*(B13), 19729–19737. https://doi.org/10.1029/92JB01594

Grindlay, N. R., & Fox, P. J. (1993). Lithospheric stresses associated with nontransform offsets of the Mid-Atlantic Ridge: Implications from a finite element analysis. *Tectonics*, *12*(4), 982–1003. https://doi.org/10.1029/93TC00364

Grindlay, N. R., Fox, P. J., & MacDonald, K. C. (1991). Second-order ridge axis discontinuities in the south Atlantic: Morphology, structure, and evolution. *Marine Geophysical Researches*, *13*(1), 21–49. https://doi.org/10.1007/BF02428194

Guillou, H., Hémond, C., Singer, B. S., & Dyment, J. (2017). Dating young MORB of the Central Indian Ridge (19°S): Unspiked K-Ar technique limitations versus 40Ar/39Ar incremental heating method. *Quaternary Geochronology*, *37*, 42–54. https://doi.org/10.1016/j.quageo.2016.10.002

Harmon, N., Rychert, C., Agius, M., Tharimena, S., Le Bas, T., Kendall, J. M., & Constable, S. (2018). Marine geophysical investigation of the chain fracture zone in the equatorial Atlantic from the PI-LAB experiment. *Journal of Geophysical Research: Solid Earth*, *123*(12). https://doi.org/10.1029/2018JB015982

Herzberg, C. (2004). Partial crystallization of mid-ocean ridge basalts in the crust and mantle. *Journal of Petrology*, *45*(12), 2389–2405. https://doi.org/10.1093/petrology/egh040

Honnorez, J., Bohlke, J. K., Honnorez-Guerstein, B. M., Dmitriev, L., & Heirtzler, J. (1978). Petrographical and geochemical study of the low temperature submarine alteration of basalt from Hole 396B, Leg 46. *Initial Reports of the Deep Sea Drilling Project*, *46*, 299–329.

Hooft, E. E. E., Detrick, R. S., Toomey, D. R., Collins, J. A., & Lin, J. (2000). Crustal thickness and structure along three contrasting spreading segments of the Mid-Atlantic Ridge, 33.5°–35°N. *Journal of Geophysical Research*, *105*(B4), 8205–8226. https://doi.org/10.1029/1999JB900442

Huang, P. Y., & Solomon, S. C. (1988). Centroid depths of mid-ocean ridge earthquakes dependence on spreading rate. *Journal of Geophysical Research*, *93*(13), 445–477. https://doi.org/10.1029/jb093ib11p13445

Jackson, D. R., Winebrenner, D. P., & Ishimaru, A. (1986). Application of the composite roughness model to high-frequency bottom backscattering. *Journal of the Acoustical Society of America*, *79*(5), 1410–1422. https://doi.org/10.1121/1.393669

Jicha, B. R., Rhodes, J. M., Singer, B. S., & Garcia, M. O. (2012). ^{40} Ar/^{39} Ar geochronology of submarine Mauna Loa volcano, Hawaii: ^{40} AR/^{39} AR Geochronology of Mauna Loa. *Journal of Geophysical Research*, *117*(B9). https://doi.org/10.1029/2012JB009373

Jourdan, F., Renne, P. R., & Reimold, W. U. (2009). An appraisal of the ages of terrestrial impact structures. *Earth and Planetary Science Letters*, *286*(1–2), 1–13. https://doi.org/10.1016/j.epsl.2009.07.009

Jourdan, F., Sharp, W. D., & Renne, P. R. (2012). 40Ar/39Ar ages for deep (~3.3 km) samples from the Hawaii scientific drilling project, Mauna Kea volcano, Hawaii. *Geochemistry, Geophysics, Geosystems*, *13*(5), Q05004. https://doi.org/10.1029/2011GC004017

Karson, J. A., & Dick, H. J. B. (1983). Tectonics of ridge-transform intersections at the Kane fracture zone. *Marine Geophysical Researches*, *6*(1), 51–98. https://doi.org/10.1007/BF00300398

Karson, J. A., Karson, J. A., Fox, P. J., Sloan, H., Crane, K. T., Kidd, W. S. F., et al. (1984). The geology of the oceanographer transform: The ridge-transform intersection. *Marine Geophysical Researches*, *6*(2), 109–141. https://doi.org/10.1007/BF00285956

Klein, E. M., & Langmuir, C. H. (1987). Global correlations of ocean ridge basalt chemistry with axial depth and crustal thickness. *Journal of Geophysical Research*, *92*(B8), 8089–8115. https://doi.org/10.1029/JB092iB08p08089

Koppers, A. A. P. (2002). ArArCALCFsoftware for 40Ar/39Ar age calculations.

Langmuir, C. H., & Bender, J. F. (1984). The geochemistry of oceanic basalts in the vicinity of transform faults: Observations and implications. *Earth and Planetary Science Letters*, *69*(1), 107–127. https://doi.org/10.1016/0012-821X(84)90077-3

Langmuir, C. H., Klein, E. M., & Plank, T. (1992). Petrological systematics of mid-ocean ridge basalts: Constraints on melt generation beneath ocean ridges. In J. P. Morgan, D. K. Blackman, & J. M. Sinton (Eds.), *Geophysical monograph series* (pp. 183–280). American Geophysical Union. https://doi.org/10.1029/GM071p0183

Lawson, K., Searle, R. C., Pearce, J. A., Browning, P., & Kempton, P. (1996). Detailed volcanic geology of the MARNOK area, Mid-Atlantic Ridge north of Kane transform. *Geological Society, London, Special Publications*, *118*(1), 61–102. https://doi.org/10.1144/GSL.SP.1996.118.01.05

Lee, C.-T. A., Luffi, P., Plank, T., Dalton, H., & Leeman, W. P. (2009). Constraints on the depths and temperatures of basaltic magma generation on Earth and other terrestrial planets using new thermobarometers for mafic magmas. *Earth and Planetary Science Letters*, *279*(1–2), 20–33. https://doi.org/10.1016/j.epsl.2008.12.020

Le Voyer, M., Cottrell, E., Kelley, K. A., Brounce, M., & Hauri, E. H. (2015). The effect of primary versus secondary processes on the volatile content of MORB glasses: An example from the equatorial Mid-Atlantic Ridge (5°N–3°S). *Journal of Geophysical Research: Solid Earth*, *120*(1), 125–144. https://doi.org/10.1002/2014JB011160

Ligi, M., Bonatti, E., Cipriani, A., & Ottolini, L. (2005). Water-rich basalts at mid-ocean-ridge cold spots. *Nature*, *434*(7029), 66–69. https://doi.org/10.1038/nature03264

Ligi, M., Cuffaro, M., Chierici, F., & Calafato, A. (2008). Three-dimensional passive mantle flow beneath mid-ocean ridges: An analytical approach. *Geophysical Journal International*, *175*(2), 783–805. https://doi.org/10.1111/j.1365-246X.2008.03931.x

Lonsdale, P. (1978). Near-bottom reconnaissance of a fast-slipping transform fault zone at the Pacific-Nazca plate boundary. *The Journal of Geology*, *86*(4), 451–472. https://doi.org/10.1086/649712

Lurton, X., Lamarche, G., Brown, C., Lucieer, V., Schimel, A., & Weber, T. (2015). Backscatter measurements by seafloor-mapping sonars.

Macdonald, K. C., & Luyendyk, B. P. (1977). Deep-tow studies of the structure of the Mid-Atlantic Ridge crest near lat 37°N. *Geological Society of America Bulletin*, *88*(5), 621. https://doi.org/10.1130/0016-7606(1977)88<621:DSOTSO>2.0.CO;2

Magde, L. S., & Smith, D. K. (1995). Seamount volcanism at the Reykjanes ridge: Relationship to the Iceland hot spot. *Journal of Geophysical Research*, *100*(B5), 8449–8468. https://doi.org/10.1029/95JB00048

Maia, M., & Brunelli, D. (2020). The eastern Romanche ridge-transform intersection (equatorial Atlantic): Slow spreading under extreme low mantle temperatures. Preliminary results of the SMARTIES cruise. *EGU General Assembly Conference Abstracts*, 10314. https://doi.org/10.5194/egusphere-egu2020-10314

Maia, M., Brunelli, D., Grenet, L., Briais, A., & Hamelin, C. (2023). SMARTIES cruise - Nautile videos of the axial domain of the Mid-Atlantic Ridge south of the Romanche transform fault [Dataset]. *SEANOE*. https://doi.org/10.17882/95946

Maia, M., Brunelli, D., & Ligi, M. (2019). SMARTIES cruise, RV Pourquoi pas? https://doi.org/10.17600/18001107

Mamaloukas-Frangoulis, V., Auzende, J.-M., Bideau, D., Bonatti, E., Cannat, M., Honnorez, J., et al. (1991). In-situ study of the eastern ridge-transform intersection of the Vema fracture zone. *Tectonophysics*, *190*(1), 55–71. https://doi.org/10.1016/0040-1951(91)90354-U

Marjanović, M., Singh, S. C., Gregory, E. P. M., Grevemeyer, I., Growe, K., Wang, Z., et al. (2020). Seismic crustal structure and morphotectonic features associated with the chain fracture zone and their role in the evolution of the equatorial Atlantic Region. *Journal of Geophysical Research: Solid Earth*, *125*(10), e2020JB020275. https://doi.org/10.1029/2020JB020275

Mauduit, T., & Dauteuil, O. (1996). Small-scale models of oceanic transform zones. *Journal of Geophysical Research*, *101*(B9), 20195–20209. https://doi.org/10.1029/96JB01509

Mckenzie, D., Jackson, J., & Priestley, K. (2005). Thermal structure of oceanic and continental lithosphere. *Earth and Planetary Science Letters*, *233*(3–4), 337–349. https://doi.org/10.1016/j.epsl.2005.02.005

Mendel, V., & Sauter, D. (1997). Seamount volcanism at the super slow-spreading Southwest Indian Ridge between 57°E and 70°E.

Mendel, V., Sauter, D., Rommevaux-Jestin, C., Patriat, P., Lefebvre, F., & Parson, L. M. (2003). Magmato-tectonic cyclicity at the ultra-slow spreading Southwest Indian Ridge: Evidence from variations of axial volcanic ridge morphology and abyssal hills pattern. *Geochemistry, Geophysics, Geosystems*, *4*(5), 2002GC000417. https://doi.org/10.1029/2002GC000417

Mitchell, N. C. (1993). A model for attenuation of backscatter due to sediment accumulations and its application to determine sediment thicknesses with GLORIA sidescan sonar. *Journal of Geophysical Research*, *98*(B12), 22477–22493. https://doi.org/10.1029/93JB02217

Niespolo, E. M., Rutte, D., Deino, A. L., & Renne, P. R. (2017). Intercalibration and age of the Alder Creek sanidine 40Ar/39Ar standard. *Quaternary Geochronology*, *39*, 205–213. https://doi.org/10.1016/j.quageo.2016.09.004

Olive, J.-A., & Dublanchet, P. (2020). Controls on the magmatic fraction of extension at mid-ocean ridges. *Earth and Planetary Science Letters*, *549*, 116541. https://doi.org/10.1016/j.epsl.2020.116541

Parson, L. M., Murton, B. J., Searle, R. C., Booth, D., Evans, J., Field, P., et al. (1993). En echelon axial volcanic ridges at the Reykjanes ridge: A life cycle of volcanism and tectonics. *Earth and Planetary Science Letters*, *117*(1–2), 73–87. https://doi.org/10.1016/0012-821X(93)90118-S

Peirce, C., Gardiner, A., & Sinha, M. (2005). Temporal and spatial cyclicity of accretion at slow-spreading ridges-evidence from the Reykjanes Ridge. *Geophysical Journal International*, *163*(1), 56–78. https://doi.org/10.1111/j.1365-246X.2005.02738.x

Perfit, M. R., & Chadwick, W. W. (1998). Magmatism at mid-ocean ridges: Constraints from volcanological and geochemical investigations. In W. Roger Buck, P. T. Delaney, J. A. Karson, & Y. Lagabrielle (Eds.), *Geophysical monograph series* (pp. 59–115). American Geophysical Union. https://doi.org/10.1029/GM106p0059

Phipps Morgan, J., & Chen, Y. J. (1993). The genesis of oceanic crust: Magma injection, hydrothermal circulation, and crustal flow. *Journal of Geophysical Research*, *98*(B4), 6283–6297. https://doi.org/10.1029/92JB02650

Phipps Morgan, J., & Forsyth, D. (1988). Three-dimensional flow and temperature perturbations due to a transform offset: Effects on oceanic crustal and upper mantle structure. *Journal of Geophysical Research*, *93*(B4), 2955–2966. https://doi.org/10.1029/jb093ib04p02955

Pichler, T., Ridley, W. I., & Nelson, E. (1999). Low-temperature alteration of dredged volcanics from the southern Chile ridge: Additional information about early stages of seafloor weathering. *Marine Geology*, *159*(1–4), 155–177. https://doi.org/10.1016/S0025-3227(99)00008-0

Renne, P. R., Balco, G., Ludwig, K. R., Mundil, R., & Min, K. (2011). Response to the comment by W.H. Schwarz et al. on "Joint determination of 40K decay constants and 40Ar∗/40K for the Fish Canyon sanidine standard, and improved accuracy for 40Ar/39Ar geochronology" by P.R. Renne et al. (2010). *Geochimica et Cosmochimica Acta*, *75*(17), 5097–5100. https://doi.org/10.1016/j.gca.2011.06.021

Rundquist, D. V., & Sobolev, P. O. (2002). Seismicity of mid-oceanic ridges and its geodynamic implications: A review. *Earth-Science Reviews*, *58*(1–2), 143–161. https://doi.org/10.1016/S0012-8252(01)00086-1

Schaen, A. J., Jicha, B. R., Hodges, K. V., Vermeesch, P., Stelten, M. E., Mercer, C. M., et al. (2021). Interpreting and reporting 40Ar/39Ar geochronologic data. *GSA Bulletin*, *133*(3–4), 461–487. https://doi.org/10.1130/B35560.1

Schilling, J.-G., Hanan, B. B., McCully, B., Kingsley, R. H., & Fontignie, D. (1994). Influence of the Sierra Leone mantle plume on the equatorial mid-Atlantic Ridge: A Nd-Sr-Pb isotopic study. *Journal of Geophysical Research*, *99*(B6), 12005–12028. https://doi.org/10.1029/94JB00337

Schilling, J.-G., Ruppel, C., Davis, A. N., McCully, B., Tighe, S. A., Kingsley, R. H., & Lin, J. (1995). Thermal structure of the mantle beneath the equatorial Mid-Atlantic Ridge: Inferences from the spatial variation of dredged basalt glass compositions. *Journal of Geophysical Research*, *100*(B6), 10057–10076. https://doi.org/10.1029/95jb00668

Searle, R. C., Murton, B. J., Achenbach, K., LeBas, T., Tivey, M., Yeo, I., et al. (2010). Structure and development of an axial volcanic ridge: Mid-Atlantic Ridge, 45°N. *Earth and Planetary Science Letters*, *299*(1–2), 228–241. https://doi.org/10.1016/j.epsl.2010.09.003

Sharp, W. D., & Renne, P. R. (2005). The ^{40}Ar/^{39}Ar dating of core recovered by the Hawaii scientific drilling project (phase 2), Hilo, Hawaii: ^{40}Ar/^{39}Ar dating of core. *Geochemistry, Geophysics, Geosystems*, *6*(4). https://doi.org/10.1029/2004GC000846

Singh, W. (2018). ILAB-SPARC cruise, RV Pourquoi pas ? https://doi.org/10.17600/18000528

Smith, D. K., & Cann, J. R. (1992). The role of seamount volcanism in crustal construction at the Mid-Atlantic Ridge (24°–30°N). *Journal of Geophysical Research*, *97*(B2), 1645–1658. https://doi.org/10.1029/91JB02507

Smith, D. K., Cann, J. R., Dougherty, M. E., Lin, J., Spencer, S., MacLeod, C., et al. (1995). Mid-Atlantic Ridge volcanism from deep-towed side-scan sonar. images, 25°-29°N. *Journal of Volcanology and Geothermal Research*, *67*(67), 233–262. https://doi.org/10.1016/0377-0273(94)00086-v

Spencer, S., Smith, D. K., Cann, J. R., Lin, J., & McAllister, E. (1997). Structure and Stability of non-transform discontinuities on the Mid-Atlantic Ridge between 24º N and 30º N. *Marine Geophysical Researches*, *19*(4), 339–362. https://doi.org/10.1023/a:1004200411959

Tapponnier, P., & Francheteau, J. (1978). Necking of the lithosphere and the mechanics of slowly accreting plate boundaries. *Journal of Geophysical Research*, *83*(B8), 3955–3970. https://doi.org/10.1029/JB083iB08p03955

Turrin, B. D., Gutmann, J. T., & Swisher, C. C. (2008). A 13±3 ka age determination of a tholeiite, Pinacate volcanic field, Mexico, and improved methods for 40Ar/39Ar dating of young basaltic rocks. *Journal of Volcanology and Geothermal Research*, *177*(4), 848–856. https://doi.org/10.1016/j.jvolgeores.2008.01.049

Verhoest, L. (2022). *Melting a heterogeneous Earth's mantle under an extreme thermal gradient*. Università degli studi di Modena e Reggio Emilia and Université Bretagne Occidentale.

Walowski, K. J., Kirstein, L. A., De Hoog, J. C. M., Elliott, T., Savov, I. P., Jones, R. E., & Eimf, F. (2021). Boron recycling in the mantle: Evidence from a global comparison of ocean island basalts. *Geochimica et Cosmochimica Acta*, *302*, 83–100. https://doi.org/10.1016/j.gca.2021.03.017

Wang, Z., & Singh, S. C. (2022). Seismic evidence for uniform crustal accretion along slow-spreading ridges in the equatorial Atlantic Ocean. *Nature Communications*, *13*(1), 7809. https://doi.org/10.1038/s41467-022-35459-z

Wanless, V. D., & Behn, M. D. (2017). Spreading rate-dependent variations in crystallization along the global mid ocean ridge system. *Geochemistry, Geophysics, Geosystems*, *18*(8), 3016–3033. https://doi.org/10.1002/2017GC006924

Wilson, L., Head, J. W., & Parfitt, E. A. (1992). The relationship between the height of a volcano and the depth to its magma source zone: A critical reexamination. *Geophysical Research Letters*, *19*(13), 1395–1398. https://doi.org/10.1029/92GL01073

Yeo, I. A., Devey, C. W., LeBas, T. P., Augustin, N., & Steinführer, A. (2016). Segment-scale volcanic episodicity: Evidence from the north Kolbeinsey ridge, Atlantic. *Earth and Planetary Science Letters*, *439*, 81–87. https://doi.org/10.1016/j.epsl.2016.01.029

Yeo, I. A., & Searle, R. C. (2013). High-resolution Remotely operated vehicle (ROV) mapping of a slow-spreading ridge: Mid-Atlantic Ridge 45°N: Rov mapping of a slow-spreading ridge. *Geochemistry, Geophysics, Geosystems*, *14*(6), 1693–1702. https://doi.org/10.1002/ggge.20082

Yu, Z., Singh, S. C., & Maia, M. (2023). Evidence for low Vp/Vs ratios along the eastern Romanche ridge-transform intersection in the equatorial Atlantic Ocean. *Earth and Planetary Science Letters*, *621*, 118380. https://doi.org/10.1016/j.epsl.2023.118380

Zhang, Y.-S., & Tanimoto, T. (1992). Ridges, hotspots and their interactions as observed in seismic velocity maps. *Nature*, *355*(6355), 45–49. https://doi.org/10.1038/355045a0

References From the Supporting Information

Ballard, R. D., & Moore, J. G. (1977). *Photographic atlas of the mid-Atlantic ridge rift valley: 854*. Springer-Verlag.

Cotten, J., Le Dez, A., Bau, M., Caroff, M., Maury, R. C., Dulski, P., et al. (1995). Origin of anomalous rare-earth element and yttrium enrichments in subaerially exposed basalts: Evidence from French Polynesia. *Chemical Geology*, *119*(1–4), 115–138. https://doi.org/10.1016/0009-2541(94)00102-e

Dalrymple, G. B., & Moore, J. G. (1968). Argon-40: Excess in submarine pillow basalts from Kilauea volcano, Hawaii. *Science*, *161*(3846), 1132–1135. https://doi.org/10.1126/science.161.3846.1132

French oceanographic fleet. (2023). Website of the French oceanographic fleet. Retrieved from https://www.flotteoceanographique.fr/en/Facilities/Shipboard-software/Analyse-et-traitement-de-l-information/ADELIE/Features

Gràcia, E., Bideau, D., Hekinian, R., & Lagabrielle, Y. (1999). Detailed geological mapping of two contrasting second-order segments of the Mid-Atlantic Ridge between Oceanographer and Hayes fracture zones (33°30′N-35°N). *Journal of Geophysical Research*, *104*(B10), 22903–22921. https://doi.org/10.1029/1999JB900161

Guillou, H., Nomade, S., Carracedo, J. C., Kissel, C., Laj, C., Perez Torrado, F. J., & Wandres, C. (2011). Effectiveness of combined unspiked K–Ar and 40Ar/39Ar dating methods in the 14C age range. *Quaternary Geochronology*, *6*(6), 530–538. https://doi.org/10.1016/j.quageo.2011.03.011

Katz, R. F., Spiegelman, M., & Langmuir, C. H. (2003). A new parameterization of hydrous mantle melting. *Geochemistry, Geophysics, Geosystems*, *4*(9), 2002GC000433. https://doi.org/10.1029/2002GC000433

Lee, J.-Y., Marti, K., Severinghaus, J. P., Kawamura, K., Yoo, H.-S., Lee, J. B., & Kim, J. S. (2006). A redetermination of the isotopic abundances of atmospheric Ar. *Geochimica et Cosmochimica Acta*, *70*(17), 4507–4512. https://doi.org/10.1016/j.gca.2006.06.1563

Murton, B. J., & Parson, L. M. (1993). Segmentation, volcanism and deformation of oblique spreading centres: A quantitative study of the Reykjanes ridge. *Tectonophysics*, *222*(2), 237–257. https://doi.org/10.1016/0040-1951(93)90051-K

Nomade, S., Renne, P. R., Vogel, N., Deino, A. L., Sharp, W. D., Becker, T. A., et al. (2005). Alder Creek sanidine (ACs-2): A quaternary 40Ar/39Ar dating standard tied to the Cobb mountain geomagnetic event. *Chemical Geology*, *218*(3–4), 315–338. https://doi.org/10.1016/j.chemgeo.2005.01.005

Schnur, S. R., Chadwick, W. W., Embley, R. W., Ferrini, V. L., De Ronde, C. E. J., Cashman, K. V., et al. (2017). A decade of volcanic construction and destruction at the summit of NW Rota-1 seamount: 2004–2014. *Journal of Geophysical Research: Solid Earth*, *122*(3), 1558–1584. https://doi.org/10.1002/2016JB013742

Smith, D. K., & Cann, J. R. (1999). Constructing the upper crust of the Mid-Atlantic Ridge: A reinterpretation based on the Puna ridge, Kilauea volcano. *Journal of Geophysical Research*, *104*(B11), 25379–25399. https://doi.org/10.1029/1999jb900177

Smith, D. K., Kong, L. S. L., Johnson, K. T., & Reynolds, J. R. (2002). In E. Takahashi, P. W. Lipman, M. O. Garcia, J. Naka, & S. Aramaki (Eds.), *Volcanic morphology of the submarine Puna ridge, Kilauea volcano. In geophysical monograph series*, *Geophysical Monograph series* (Vol. 128, pp. 125–142). American Geophysical Union. https://doi.org/10.1029/GM128p0125